

<https://doi.org/10.1038/s43246-025-00940-x>

Random and unpredictable optical textures in biobased self-assembled ionogels for dynamic anti-counterfeiting tags

Susana I. C. J. Palma^{1,2} , Efthymia Ramou^{1,2} & Ana C. A. Roque^{1,2} ✉

Physical unclonable function (PUF) tags generated through stochastic processes yield unique identifiers, providing secure anti-counterfeiting mechanisms for product authentication and tracking. The widespread use of PUF tags also poses environmental concerns, not only during fabrication but also upon disposal. Here, we present biobased optical materials to produce PUF tags with dual security levels by a simple and biobased process. These tags exploit the unique properties of 5CB liquid crystal, which self-assembles with ionic liquids to spontaneously form droplets within a gelatin matrix. Comprising 80% of biodegradable materials, the optical tags provide a PUF system with high encoding capacity, long-term stability, and robustness. The dynamic and unique gas-responsive properties of the optical droplets deliver dual security levels, enhanced by tamper-evident and temperature-monitoring features. Authenticity verification is straightforward via optical microscopy and can integrate AI-driven image recognition, offering superior security and tracking. This combination of high PUF security with a biobased and low-cost approach makes the system appealing across diverse markets.

Counterfeiting goods and technology is a worldwide growing business that causes trillion-dollar losses to industry¹. In Europe, the financial impact of counterfeiting goods represents 5% of the imports², and apart from the financial impact, there are also serious concerns regarding human health and security. In fact, about 10% of medicines and medical products circulating worldwide, 25% of alcohol consumed, and 10% of electrical components are counterfeits. The WHO estimated that fake medicines kill more than 250,000 children/year, and adulterated alcohol caused 3000 deaths just between 2018 and 2020.

Anti-counterfeiting tags are physical marks placed on the inside or outside of products to ensure authentication and to prevent forgery and counterfeiting. These tags contain unique identifiers that are checked against a verification system to confirm that the product is genuine. To avoid counterfeiting, the identifiers must be difficult or impossible to replicate. However, currently implemented tags as radio frequency identification (RFID) tags, holograms and watermarks, are produced by deterministic production processes, which makes them vulnerable to cloning, due to their low complexity and high predictability. Physical unclonable function (PUF)

tags are the solution for this problem because they are produced by stochastic processes and, as such, cannot be copied, not even by the manufacturer. PUF systems consist of the physical tags to apply in the products, an instrumentation component (readout device) that scans the tags to get their digital code, key or “fingerprint”, and a dedicated software for checking the authenticity of the key “fingerprint”¹.

The first PUF anti-counterfeiting tags were introduced in 2002, utilising an epoxy-polymer matrix with a random 3D pattern of glass spheres that was converted to a binary code³, serving as a unique fingerprint for the tagged object. Since then, various PUF tags have emerged, employing random patterns in substrates through methods such as the distribution of nano⁴ or microparticles^{5,6}, textural variations in paper products⁷, fingerprint-like textures^{8–10}, and random fractal networks¹¹, all detectable by the naked eye or microscopy. Enhanced security is achieved by combining multiple physico-chemical properties in a single tag, allowing the generation of multiple independent keys^{10,12} that must all be validated for authenticity. However, these systems face limitations, including low sustainability of materials, complex read-out instrumentation, reduced

¹UCIBIO—Applied Molecular Biosciences Unit, Department of Chemistry, School of Science and Technology, NOVA University Lisbon, Caparica, Portugal.²Associate Laboratory i4HB—Institute for Health and Bioeconomy, School of Science and Technology, NOVA University Lisbon, Caparica, Portugal.✉ e-mail: cecilia.roque@fct.unl.pt

durability and scalability, and restricted encoding capacity (EC) due to binary coding approaches.

Liquid crystal (LC)-based materials hold significant potential for PUF tags due to their unique optical, self-assembly and stimuli-responsive properties. The examples reported so far rely on static LC optical textures during the authentication pipeline^{6,8,9,13–16}, overlooking the LC dynamic response to external stimuli. Simultaneously, the sustainability of LC-based tags fabrication is still a concern as high temperatures^{8,9,14}, organic solvents¹⁶, and complex processes or substrates (e.g. microfabrication^{6,14}, plasma treatment^{14,15} or conductive ink screen printing⁹) are employed.

In this work, we present a generation of bio- and LC-based PUF tags relying on the spontaneous, yet dynamic and cooperative self-assembly characteristics of LCs, ionic liquids (ILs) and proteins (Fig. 1a–d). The PUF tags use the optical textures of LC droplets and their dynamic gas-response patterns for a multi-step authentication pipeline, further expanded with temperature control and tampering detection properties (Fig. 1e). Future integration with authentication tools enabled by AI-based image pattern recognition (e.g. deep learning) will offer unprecedented opportunities to develop solutions for extra-security, anti-counterfeiting and tracking options.

Results

Biobased optical ionogels using methylimidazolium chloride ILs

The physical tags used in this work consist of gel films composed of a gelatin ionogel matrix with unclonable and unpredictable optical patterns formed by spheroid microdroplets of the LC 4-Cyano-4'-pentylbiphenyl (5CB) stabilised by a surfactant IL^{17–25} from the imidazolium chloride family. These biobased optical ionogels result from the supramolecular assembly of LC and IL molecules in microdroplets dispersed within a matrix of gelatin, gelled in IL in the presence of water¹⁷ (Fig. 1a–d). The droplets' self-assembly mechanism is stochastic and uncontrollable, as it occurs spontaneously due to the interplay of hydrophobic and hydrophilic interactions between the gel components¹⁷. Upon gelation, the droplets become entrapped in the ionogel matrix, yielding unique optical patterns with potential to be used as authentication tags with two levels of security, temperature control and anti-tamper features (Fig. 1e).

Initially, to tune the optical ionogel formulation for PUF tags, we started by screening a set of imidazolium chloride ILs (C_n mimCl) with alkyl chain lengths (n) between 2 and 12 carbons (Fig. 1c).

The ILs with shorter alkyl chains ($n = 2, 4$, and 6 carbons) produced ionogels with LC droplets but distinct viscoelastic features (Fig. 2a–c), which can be attributed to the increasing hydrophobic character of the ILs. The C_2 mimCl is the most hydrophilic of the three ILs and behaves like a salt due to its short alkyl chain, generating solid-like ionogels that entrap the LC droplets. In the C_n mimCl series, C_4 mimCl and C_6 mimCl have an intermediate behaviour between salts and surfactants, self-assembling into structures such as bilayers, which are known to interfere with the gelatin hydrogen bond-mediated crosslinking²⁶. The C_4 and C_6 ionogels obtained with these ILs are fluid (Fig. 2b, c), probably due to crosslinking limitations, and are unable to immobilise LC droplets. Given this instability, C_4 and C_6 ionogel films (Supplementary Fig. S1) were discarded as potential PUF tags.

For the long alkyl chain ILs ($n = 8, 10$ and 12 carbons), it was impossible to produce optical ionogels using composition ratios identical to those used in C_2 , C_4 and C_6 formulations (Supplementary Fig. S2a). Under such high concentrations, C_8 , C_{10} and C_{12} mimCl alone, self-assemble into gels and/or LC phases^{27–29}. After fine-tuning the molar ratios of IL, LC, gelatin and water (Supplementary Fig. S2a, c), we could prepare solid-like optical ionogels with immobilised LC droplets using the three long alkyl chain ILs ($n = 8, 10$ and 12 carbons) (Fig. 2d–f). Unfortunately, for C_{10} mimCl, this result was difficult to reproduce because C_{10} mimCl is highly hygroscopic and readily uptakes humidity from the environment during handling at room conditions, forming a gel-like LC phase²⁹ that hampers the preparation of an optical ionogel. Additionally, when the optical ionogel preparation was successful, the C_{10} films contained only a small population of droplets compared to the C_8 and C_{12} films (Table S1), suggesting that, for

this formulation, IL-water, IL-IL or IL-gelatin interactions are preferred as compared to IL-LC. Thus, the C_{10} formulation was discarded as a potential PUF tag (Supplementary Fig. S1).

In summary, only the formulations containing C_n mimCl ILs with $n = 2, 8$ and 12 carbons formed reproducible self-supporting gels (C_2 , C_8 and C_{12}) that do not flow upon inversion (Fig. 2a, d, f) and contain large populations of LC droplets forming unpredictable optical texture patterns (Table S1 and Fig. 2a, d, f). As such, these were considered more promising for PUF tag applications and were further investigated in the following sections.

To study the viscoelastic, structural and air-stability properties of C_2 , C_8 and C_{12} optical ionogels we prepared the following control formulations for reference: (i) a gelatin hydrogel (composed of only gelatin and water); and (ii) three gelatin ionogels, one for each IL (composed by gelatin, IL and water) (Supplementary Fig. S2b, d). The oscillatory shear measurements confirmed that C_2 , C_8 and C_{12} optical ionogels present a solid-like behaviour, as their storage *moduli*, G' , are about one order of magnitude larger than their loss *moduli* G'' , both independent of the frequency (Fig. 3a, Supplementary Fig. S3a, and Table S2). C_2 is the softest gel (with G' and G'' of 10^3 Pa and 10^2 Pa, respectively) which can be attributed to its higher content in IL and lower water content when compared to C_8 and C_{12} (Supplementary Fig. S2a, c). The higher water content of C_8 and C_{12} optical ionogels probably explains their G' and G'' *moduli* (10^4 Pa and 10^3 Pa, respectively) being closer to those of the hydrogel (Fig. 3a).

The C_2 , C_8 and C_{12} ionogels yielded X-ray diffraction images with a diffuse ring around 4 Å (Fig. 3b–d), also visible in the hydrogel (Fig. 3e), which is associated with the amorphous regions of the gelatin biopolymer, composed of random coils of polypeptide chains, without structural ordering^{17,20}. However, the ring at 12 Å present in the control hydrogel (Fig. 3e) due to the polypeptide chain packing as triple helices³⁰ is lacking in C_2 , C_8 and C_{12} (Fig. 3b–d) and in the respective control ionogels (Supplementary Fig. S3i–k). This indicates that the IL suppresses the assembly of gelatin polypeptide chains into triple helices, in accordance with previous studies^{17,20}. Such suppression occurs because the IL interacts with the polypeptide chains (namely through ionic, electrostatic, hydrophobic and H-bonds) and interferes with the hydrogen bond network that is responsible for the packing of the triple helices²⁶ and gel strength. Interestingly, for C_8 and C_{12} optical ionogels (Fig. 3c, d) and their ionogel controls (Supplementary Fig. S3j, k) there is an extra diffraction ring at around 26 Å and 29 Å, respectively, which is not present in the hydrogel (Fig. 3e), suggesting the existence of order derived from the IL organisation, similar to the previously described fibroin ionogels in C_6 mimCl and C_{10} mimCl³¹. Since the IL concentrations in these ionogels are lower than their lyotropic ranges^{27,28}, other levels of organisation could be present due to IL self-assembly, such as an IL micellar cubic phase, as suggested by Coarse Grain simulation of C_8 mimCl aqueous solutions 37% w/w³², identical to the ratios used in this work.

To study the air-stability of C_2 , C_8 and C_{12} optical ionogels, we moulded them as discs and stored them at ambient conditions (RH = 52 ± 3 % and $T = 22 \pm 1$ °C), while monitoring their weight for 30 days (Fig. 3f and Supplementary Fig. S2e). Water evaporation caused a major weight loss in the first 3 days of storage (−5% for C_2 , −40% for C_8 , −60% for C_{12} and −70% for the hydrogel), after which the weight remained stable, indicating that the water content in these formulations rapidly equilibrates with the environment. The lowest weight loss was observed for C_2 , attributable to the initially lower water content of C_2 compared to C_8 and C_{12} (Supplementary Fig. S2a, c). The three ionogel samples maintain a solid-like character after the initial 3-day equilibration period. However, some textural changes were observed, that are likely associated with the water content variations (for example, C_2 became sticky and C_8 became irreversibly deformable). The C_{12} sample, despite shrinking and losing some deformability (Fig. S3c, d), remained sufficiently flexible, without breaking when manually bending, unlike the hydrogel with similar water content (Fig. 3g). Tensile tests confirmed that this aged C_{12} sample was remarkably tougher than the fresh one, with fracture strength and strain increasing dramatically from 10 kPa

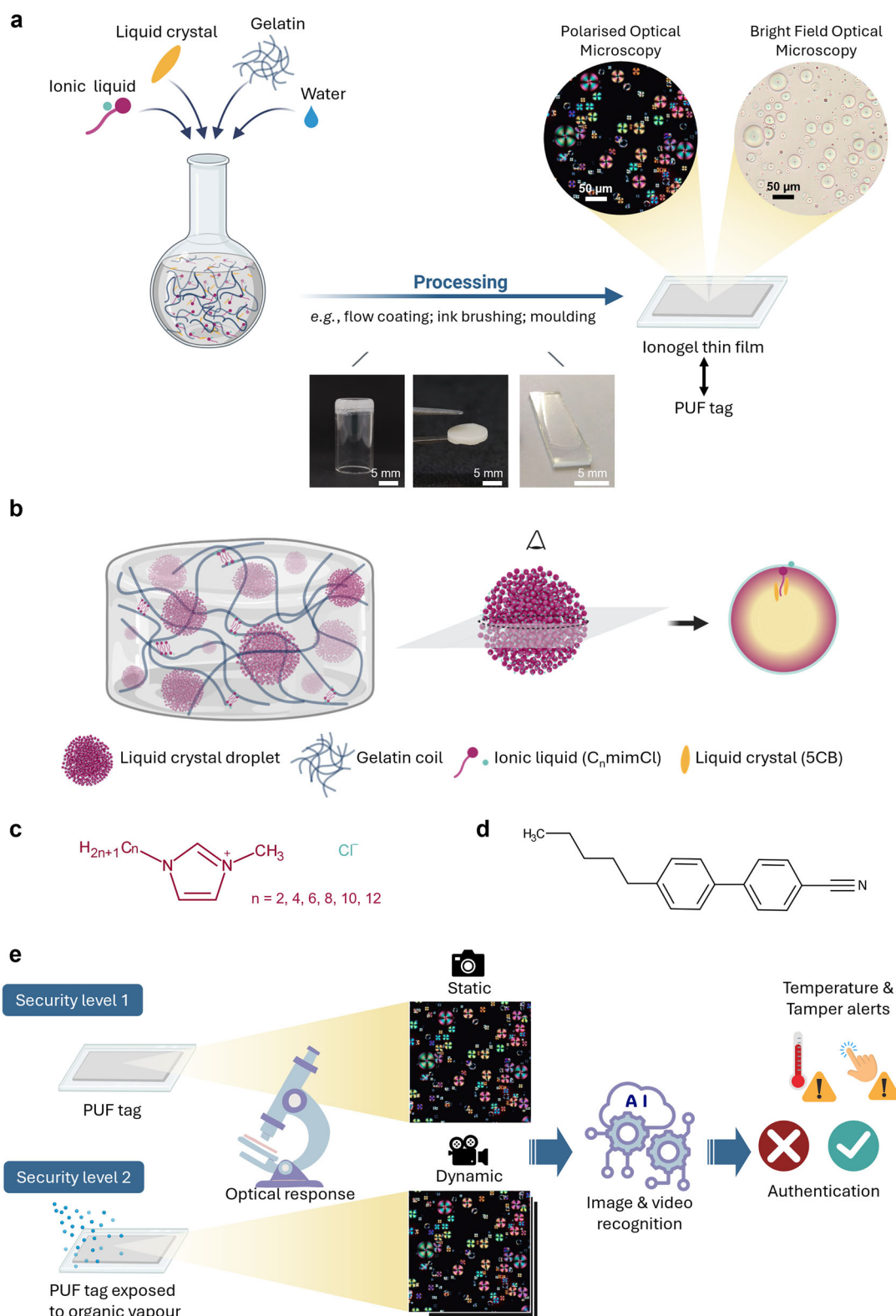


Fig. 1 | PUF tags prepared from biobased optical ionogel films. a One-pot preparation of the optical ionogel, respective macroscopic aspect and processing as a film to form the PUF tag. **b** Schematic representation of the supramolecular organisation of the optical ionogel embedding LC droplets, where LC molecules are confined inside a spheroid shell formed by imidazolium chloride IL molecules. The transversal cut of the droplet illustrates the perpendicular anchoring of the LC molecules at the surface of the droplet, promoted by the IL. **c** Chemical structure of the molecules of imidazolium chloride IL ($C_n\text{mimCl}$). **d** Chemical structure of the

LC 4-Cyano-4'-pentylbiphenyl (5CB). **e** Dual-step authentication pipeline, where 2 security levels must be verified for authentic tags: (i) authenticity of the static optical texture observed under polarised optical microscopy (POM); and (ii) authenticity of the dynamic POM patterns as a response to a defined organic vapour. This dual-step verification is performed by a pre-trained cloud-based AI algorithm, also enabled with the ability to detect if the tag was exposed to undue temperatures or suffered from tampering. Created in BioRender. Roque, C. (2025) <https://BioRender.com/r68r365>.

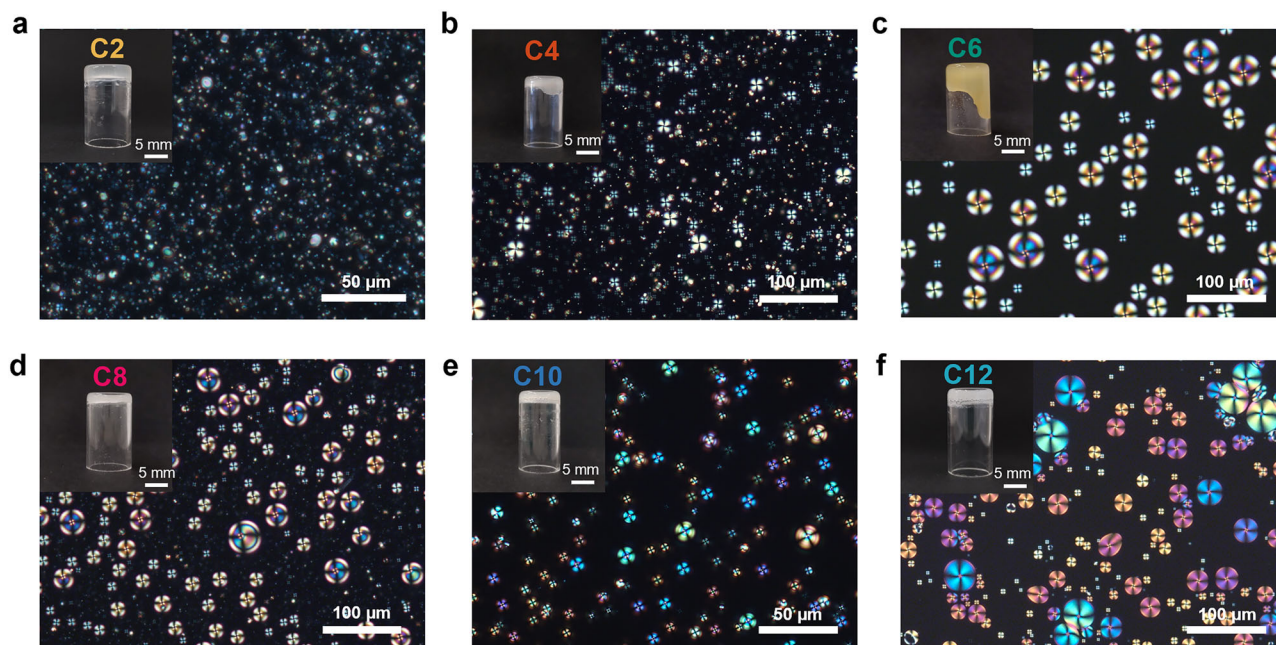


Fig. 2 | Macroscopic and microscopic aspects of the biobased optical ionogels prepared with C_n mimCl ILs, water, gelatin and the 5CB LC. a–f POM images, with polarisers crossed at 90° , of optical ionogel films prepared with C_2 , C_4 , C_6 , C_8 ,

C_{10} and C_{12} mimCl, respectively. The insets show inverted glass vials containing the ionogels.

and 68% to 3.1 MPa and 90.5%, respectively (Supplementary Fig. S3d). Regarding the response to shear stresses, there was an increase of 3 orders of magnitude in G' and G'' (Fig. 3h and Supplementary Fig. S3b) when compared to the fresh sample. It is expected that these mechanical properties are maintained for longer periods, following the observed stability of gel weight for 1 year (Supplementary Fig. S2f).

Optical textures and topography of biobased optical ionogel films

When the optical ionogels C_2 , C_8 and C_{12} are processed as films, the LC droplets are randomly distributed over the film area and are visible by optical microscopy, typically with a magnification larger than $5\times$ (Fig. 4a–f). The average droplet diameter varies between $6\mu\text{m}$ in C_2 , $16\mu\text{m}$ in C_8 and $20\mu\text{m}$ in C_{12} (Fig. 4g–i), and the droplet populations are polydisperse (polydispersity of 0.53, 0.34 and 0.44 in C_2 , C_8 and C_{12} , respectively, Fig. 4g–i). This is due to the stochastic mechanism of the droplets' self-assembly, which prevents the precise control of droplet sizes. In each film, a variety of droplet sizes is usually found, which is important to create the morphological variability and randomness required for safe PUF tags.

The films produced with C_2 optical ionogel exhibit bipolar LC droplets characterised by two surface point defects located at opposite poles of the droplet (visualised in BF) and an optical texture that changes upon rotation in POM with respect to the crossed polarisers (Fig. 4a, d), which is characteristic of a tangential anchoring of the LC molecules to the droplet interface³³. C_2 mimCl behaves more like a salt than as a surfactant and its short alkyl chain cannot provide a perpendicular anchoring to the LC molecules nor stabilise the droplets surface, leading to irregular shapes in some droplets (as seen in AFM images, Fig. 4j). After one week of storage at room conditions, LC leaking to the gelatin matrix is observed, probably due to droplets disassembly (Supplementary Fig. S4).

A balance of intermolecular interactions is required to produce ionogel films embedding immobilised, stable, and oriented LC droplets. This was better achieved with the C_8 and C_{12} formulations. In these cases, the amphiphilic and surface-active character of the IL^{28,34} promotes the stable compartmentalisation of water-soluble and insoluble components of the gel, generating droplets that encapsulate the hydrophobic LC molecules, further immobilised in the ionogel gelatin matrix. Importantly, the long alkyl chains

of the IL cation induce the homeotropic (or perpendicular) anchoring of the LC at the droplets interface³³. This results in oriented LC droplets, with director profiles typically radial (exhibiting a Maltese cross pattern in POM and a central core defect visualised in BF) and escaped radial (showing a distorted Maltese cross with an off-centre defect) in C_8 films (Fig. 4b, e). In the case of C_{12} films, radial and twisted radial droplets are observed (Fig. 4c, f). The twisted radial is a variant of the radial droplet with a small twist at the centre. This deformation occurs to reduce the core defect energy in radial droplets³⁵. In general, in C_{12} films, the droplet colours are similar when sizes are similar, but we found some exceptions (for example, droplets between $14\mu\text{m}$ and $22\mu\text{m}$ in diameter can be either purple or orange (Supplementary Fig. S5a, b)). It is known that droplet configurations are affected by several factors, including boundary conditions, droplet size and shape³³. Here, the different colours arise, probably, from the fact that the droplet population is not perfectly spherical, instead, spheroid and flat pancake-like shapes have been observed (Fig. 4l and Supplementary Fig. S5k), in accordance with our previous findings for similar gelatin ionogel matrices embedding 5CB droplets¹⁹. A third droplet profile is also observed, featuring a bright peripheral ring with short extinction bands that match the direction of the crossed polarisers and a central pseudo-isotropic region, which remains dark upon rotation (Fig. 4c and Supplementary Fig. S5h), while BF photos reveal a circular defect in some of the droplets (Fig. 4f and Supplementary Fig. S5i). Based on further investigations, we have concluded that the optical textures in BF are not a lensing effect, instead, these structures could be attributed to an axial director configuration with a disclination loop, probably close to the equator^{36–38}. Here, the droplet pole, or axis, is perpendicular to the field of view³⁹ (Fig. 4c, f and Supplementary Fig. S5g–i). An axial director profile can be observed in droplet systems with weak anchoring, which can decrease the energy of the structure by allowing a tilt in the LC alignment at the droplet interface^{35,36,40,41}. We propose that the axial configuration arises from the fact that the C_{12} mimCl IL provides sufficiently weak anchoring that facilitates this droplet organisation. For sufficiently weak anchoring energies, there are no defects in this structure, but for stronger anchoring conditions, an equatorial disclination can occur^{35,39}. Raman mapping of the surface of the films showed a uniform distribution of the 5CB $C\equiv N$ stretching vibration peak (2227 cm^{-1}) at the surface of the axial droplet (Supplementary Fig. S5j), which is consistent

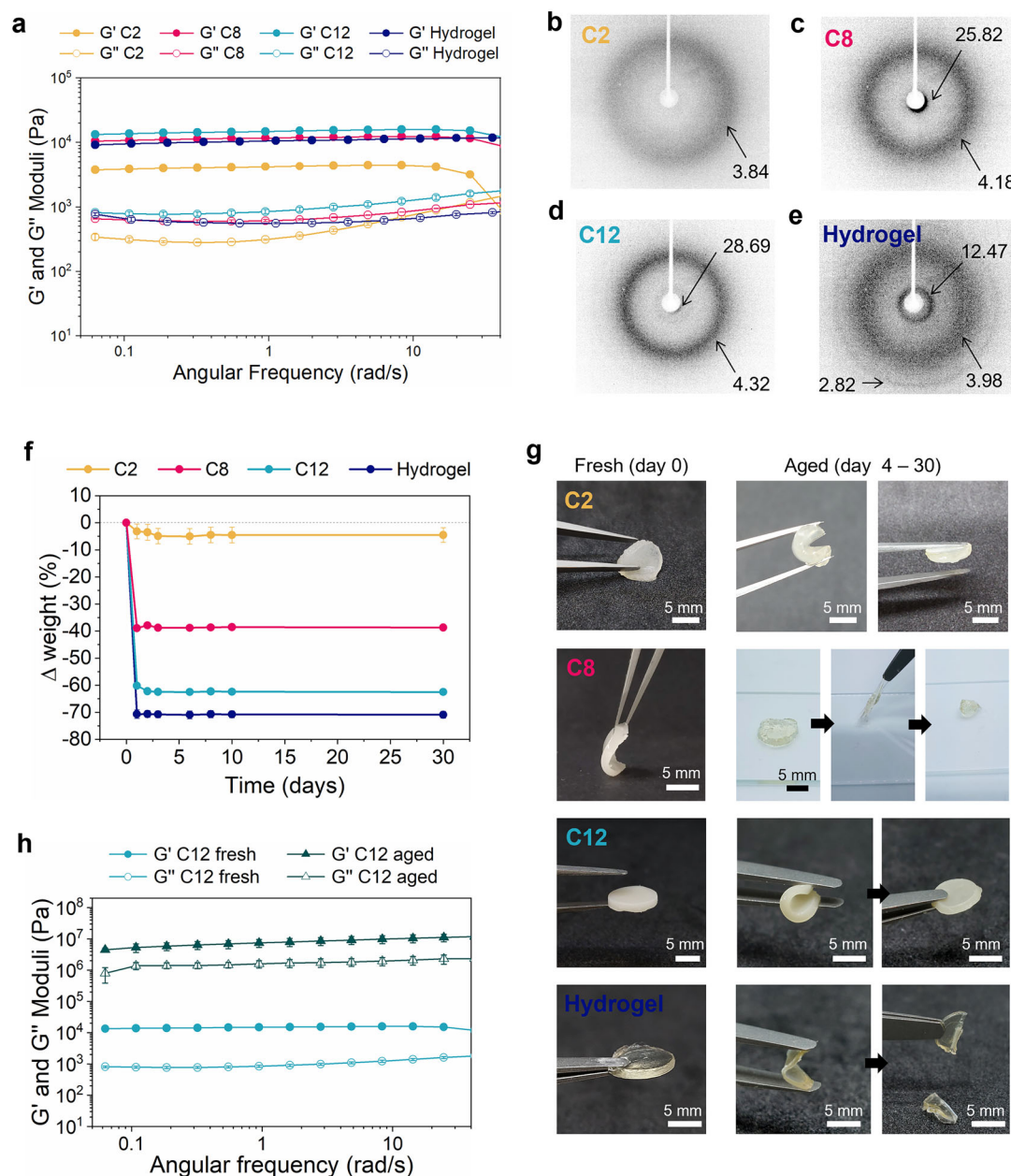


Fig. 3 | Viscoelastic, structural and air-stability properties of the biobased optical ionogels. **a** Frequency sweep measurement revealing the viscoelastic properties (shear storage (G') and loss (G'') moduli) of C2, C8 and C12 optical ionogels and a control gelatin hydrogel. Data shown corresponds to the average moduli values for $n = 2$ replicate samples; the error bars represent the standard deviation. Individual plots for the replicates can be found in the Supplementary Fig. S3. **b–e** X-ray scattering images and distances (in Å) of the characteristic diffraction rings of C2, C8, C12 optical ionogels and control hydrogel. **f** Variation of optical ionogels and control hydrogel weight during storage at room conditions ($22 \pm 1^\circ\text{C}$ and $52 \pm 3\%$ RH) for 30 days; data, error bars are represented as in (a). Individual plots for the

replicates can be found in the Supplementary Fig. S2. **g** Macroscopic aspect of the fresh (day 0) and aged optical ionogels, where the morphological aspect of the aged sample is identical between day 4 and day 30 of storage at room conditions. **h** Frequency sweep measurements of the C12 optical ionogel in fresh (day 0) and aged (day 30) conditions, performed with strains of 0.05 and 0.00005 for the fresh and aged sample, respectively, within the linear viscoelastic region of each sample (as determined in Fig. S3b); data and error bars are presented as in (a) and individual plots for the replicates can be found in the Supplementary Fig. S3. In all figures, the hydrogel is composed of only gelatin and water, as represented in Supplementary Fig. S2d.

with the perpendicular alignment of the 5CB molecules with the nitrile group facing the droplet interface, when the droplet pole is perpendicular to the field of view. For radial droplets, the Raman maps are totally different, showing a preferential distribution of the 5CB $\text{C}\equiv\text{N}$ stretching vibration peak in two diametral opposite areas of the droplet surface spreading radially from the surface to the centre of the droplet (Supplementary Fig. S5f).

Air-stability of the optical textures of biobased optical ionogel films

Regarding the shape and stability of the droplets, we observed that, unlike in the C2 films, droplets in C8 and C12 films appear as symmetrical semi-spherical protuberances in the AFM images of the film surface (Fig. 4j–l). Additionally, no LC leaking or droplet coalescence was observed during exposure to room conditions for 4 weeks in C8 films (Supplementary

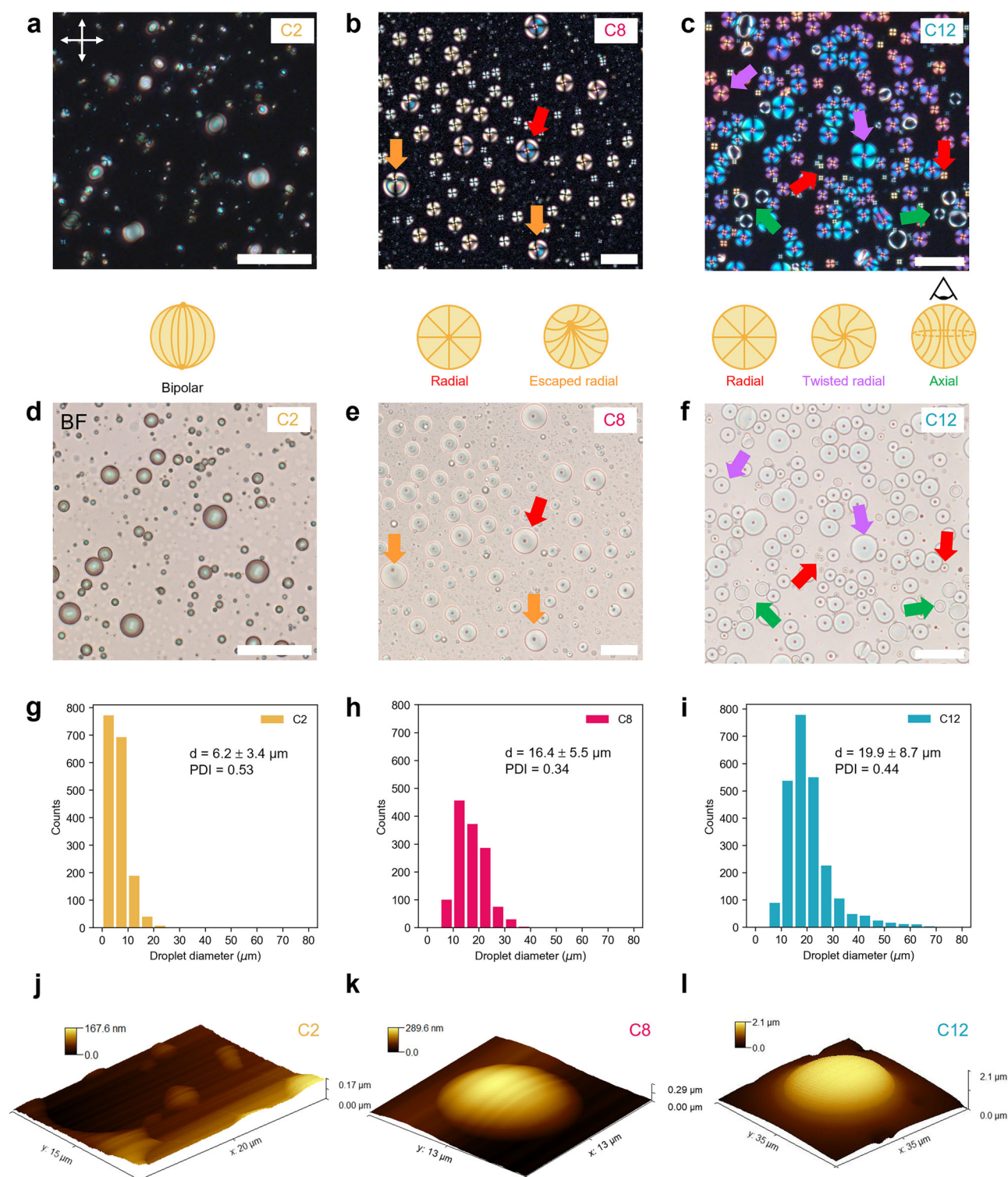


Fig. 4 | Microscopic morphology and topography of films prepared with C2, C8 and C12 biobased optical ionogels. **a–c** POM images and schematic representation of the LC director profiles of the droplets found in, respectively, C2, C8 and C12 films formed on top of glass slides. The red arrows indicate examples of radial droplets, the orange arrows indicate examples of escaped radial droplets, the purple arrows indicate examples of twisted radial droplets, and the green arrows indicate examples of axial droplets, where the droplet pole is perpendicular to the field of view. **d–f** Corresponding BF microscopy images of the films in (**a–c**). The scale bar in the optical microscopy images represents 50 μm . **g–i** Size distribution of droplets found in C2, C8 and C12 films, respectively. The histograms, the average and the

standard deviation diameters were calculated for a large population of droplets (at least 1300 droplets) measured in at least 8 different regions of interest (ROI) of BF images of at least 2 independent films (C2: $n = 2$ films, 8 ROIs, total 1699 droplets; C8: $n = 3$ films, 9 ROIs, total 1323 droplets; C12: $n = 7$ films, 9 ROIs; total 2440 droplets). Polydispersity Index (PDI) was calculated as the ratio between the diameter standard deviation and the average diameter. **j–l** Atomic force microscopy (AFM) images (height retrace mode) showing the topography of the films' surface and representative droplets (droplets with the most frequent diameter) found in each formulation (C2: 4 μm ; C8: 10 μm ; C12: 20 μm , according to the size distribution histograms in (**g–i**).

Fig. S6) and for 4 years in C12 films (Fig. 5a, b). This can be attributed to the strong stabilising interfaces formed by the C_8mimCl and $C_{12}mimCl$ ILs²⁰.

For the application of optical ionogel films as PUF tags, the long-term stability of droplets is a critical factor. Typically, LC droplets in aqueous emulsions are mobile and undergo coalescence, sedimentation or Ostwald ripening⁴². Adding a support matrix material, such as a gelatin gel, adds stability to the system. In the case of C12 films, the stability is remarkable. Indeed, the C12 films embed and immobilise LC droplets with high stability, even when stored for long periods at room conditions (Fig. 5). During 4 years of storage (RH = $54 \pm 11\%$ and $T = 22 \pm 1^\circ C$) the POM

and BF images of a C12 film remain morphologically similar ($94 \pm 4\%$ and $86 \pm 6\%$ average similarity, respectively, calculated by the FSIM algorithm⁴³) (Fig. 5c, d), as the droplets do not coalesce, and maintain their positions (Fig. 5a, b). At the droplet interface, the ionic interactions between the imidazolium ring of the cation $C_{12}mim^+$ and the Cl^- anion, the $Cl^- \cdots OH$ hydrogen bonds with water molecules and the electrostatic interactions with charged groups of gelatin likely aid in the droplet immobilization²⁰. Regarding the LC configuration, the twisted radial LC director profile is stable at least up to the second year of storage (Fig. 5a), and the subtle colour changes observed during this period could be

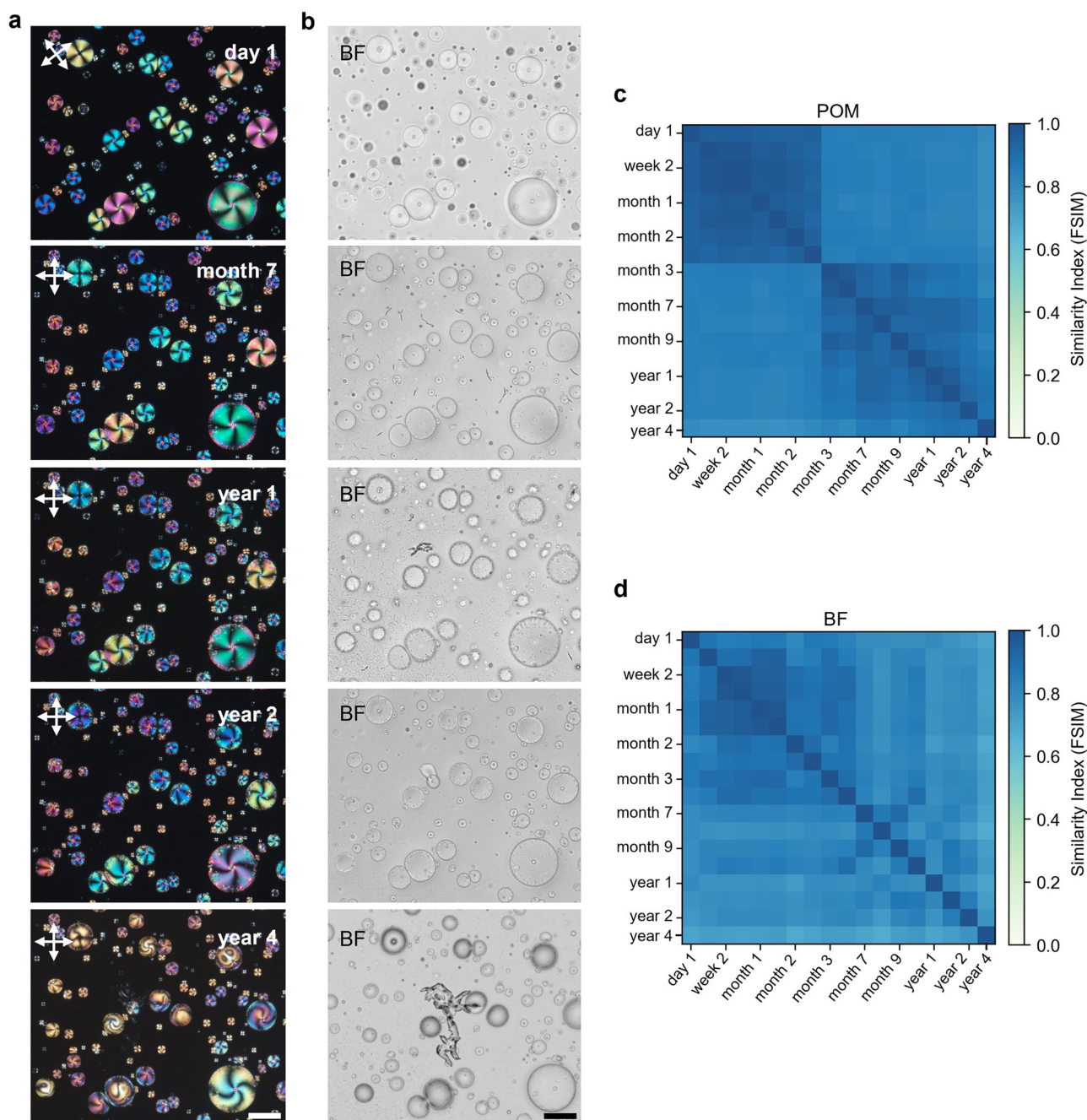


Fig. 5 | Long-term morphological stability of C12 films stored at room conditions (RH = $54 \pm 11\%$; $T = 22 \pm 1^\circ C$). **a** Representative POM images of a C12 film region over 4 years. **b** Corresponding BF microscopy images. Scale bar represents 50 μm . **c** Similarity matrix for POM images over 4 years, where each cell, m_{ij} , represents the FSIM (feature similarity index) calculated between a photo taken at

time point i and another photo of the same region taken at time j (FSIM = 0.96 ± 0.05 in the first 2.5 months and FSIM = 0.91 ± 0.05 between month 3 and year 4). **d** Corresponding BF similarity matrix (FSIM = 0.90 ± 0.02 in the first 2.5 months and FSIM = 0.82 ± 0.07 between month 3 and year 4).

Table 1 | Properties of fresh (24 h post-preparation) and aged (after storage at RH = 54 ± 11% and T = 22 ± 1 °C, between 4 days and 30 days) optical ionogels C2, C8, C12, C2_a and C8_a

Optical ionogel	As-prepared		Aged	
	Optical textures		Optical textures stability	
	LC droplets configuration	LC droplets population density (droplets/mm ²)	Mechanical robustness	Environmental stability
C2	Bipolar	1454 ± 304	Solid-like gel, reversibly deformable	Softer and sticky, solid-like gel; reversibly deformable Stable weight in 3 days
C8	Pre-radial and radial	243 ± 101		Softer, solid-like gel; irreversibly deformable
C12	Radial, twisted radial and axial	464 ± 165		Harder, solid-like gel; reversibly deformable
C2_a	n.a.	n.a.	2 years	
C8_a	Pre-radial and radial	218 ± 28	n.a.	
			≥ 2.5 months	

associated with changes in tilting of the LC molecules caused by fluctuations in room temperature or humidity over long periods of time.

Between month 2 and month 3 of storage the microscope’s polarisers were manually rotated, which resulted in the rotation of the droplets’ extinction bands in the POM images from month 3 onwards (Fig. 5a). The FSIM index perfectly captured the change in the POM images due to the rotated extinction bands, as highlighted in the POM similarity matrix (Fig. 5c). Namely, there are two blocks of high FSIM, the first corresponding to the POM images acquired in the first 2.5 months of storage, and the second to images acquired from month 3 onwards. The FSIM index calculated between an image acquired before 2.5 months and another acquired after 3 months of storage is lower ($83 \pm 2\%$) than if calculated between images acquired within the first 2.5 months of storage ($96 \pm 5\%$) or from month 3 onwards ($91 \pm 5\%$), due to the difference in the position of the extinction bands. Since the BF images are not affected by the polarisers’ rotation, the BF similarity matrix (Fig. 5d) does not show evidence of this hardware alteration in the system.

Investigation of biobased optical ionogel formulations with the C12 molar composition

As the C12 formulation appeared as the most robust, we reproduced its molar composition with the ILs C₂mimCl and C₈mimCl, to systematically assess the impact of the IL on the properties of the resulting materials. We obtained gels (named as C2_a and C8_a, respectively) with solid-like characteristics identical to C12 ($G' \sim 10^4$; $G'' \sim 10^3$) and identical air-stability (Supplementary Fig. S7). These materials rapidly equilibrate their water content with the environment by evaporation (between 55% and 65% of weight loss) during the first three days in room conditions and remain stable afterwards (Supplementary Fig. S7b, e), although stiffer than on the production day (Supplementary Fig. S7b). The main impact of changing the IL on the formulation is on the optical properties of the resulting films. With C₂mimCl, it was impossible to obtain droplets, likely due to the combined effect of the low stabilising properties of the IL and inadequate ratio of LC to water (Supplementary Fig. S8a, b). Thus, this formulation is not suitable for preparing PUF tags. With C₈mimCl, the films exhibited optical textures containing polydisperse populations of radial and escaped radial droplets (218 ± 28 droplets/mm²; PdI = 0.46, Supplementary Fig. S8c–e) that are stable for at least 2.5 months (Supplementary Fig. S9). Thermal investigations showed that in these C₈mimCl-based films, the radial and escaped radial droplets configuration is recovered after isotropisation (at 33 °C) and subsequent cooling to room temperature (23 °C) (Supplementary Fig. S10), in accordance with our previous studies with similar optical gels¹⁷. Despite being an interesting property, it is disadvantageous to develop PUF tags with temperature control applications, as it does not provide evidence on past exposure to high temperatures.

Selection of the best formulation for PUF tags

Table 1 summarises the properties of the biobased optical ionogel formulations prepared in this work, highlighting the parameters considered more relevant to prepare PUF tags: optical textures, mechanical robustness and environmental stability (in fresh and aged materials).

C12 optical ionogels are the most mechanically robust of the tested formulations as, unlike C2 and C8, they maintain a solid-like and reversibly deformable character even after prolonged exposure (30 days) to room conditions (Fig. 3g). Despite becoming stiffer (Fig. 3h) due to water loss in the three first days of exposure to room conditions (Fig. 3f), C12 optical ionogels remain easy to handle and maintain their integrity (Fig. 3g). Importantly, when processed as films, C12 optical ionogels exhibit very interesting optical textures (composed by three different types of LC droplet configuration—Fig. 4c, f and Table 1) which are stable for long periods (at least 2 years) in room conditions (Table 1 and Fig. 5). The high diversity of optical textures in C12 films is regarded as an advantage for PUF tags development as it decreases the predictability of the system, while stability is crucial for a durable tag. The C2 and C8 films do not fulfil the criteria of diversity and stability.

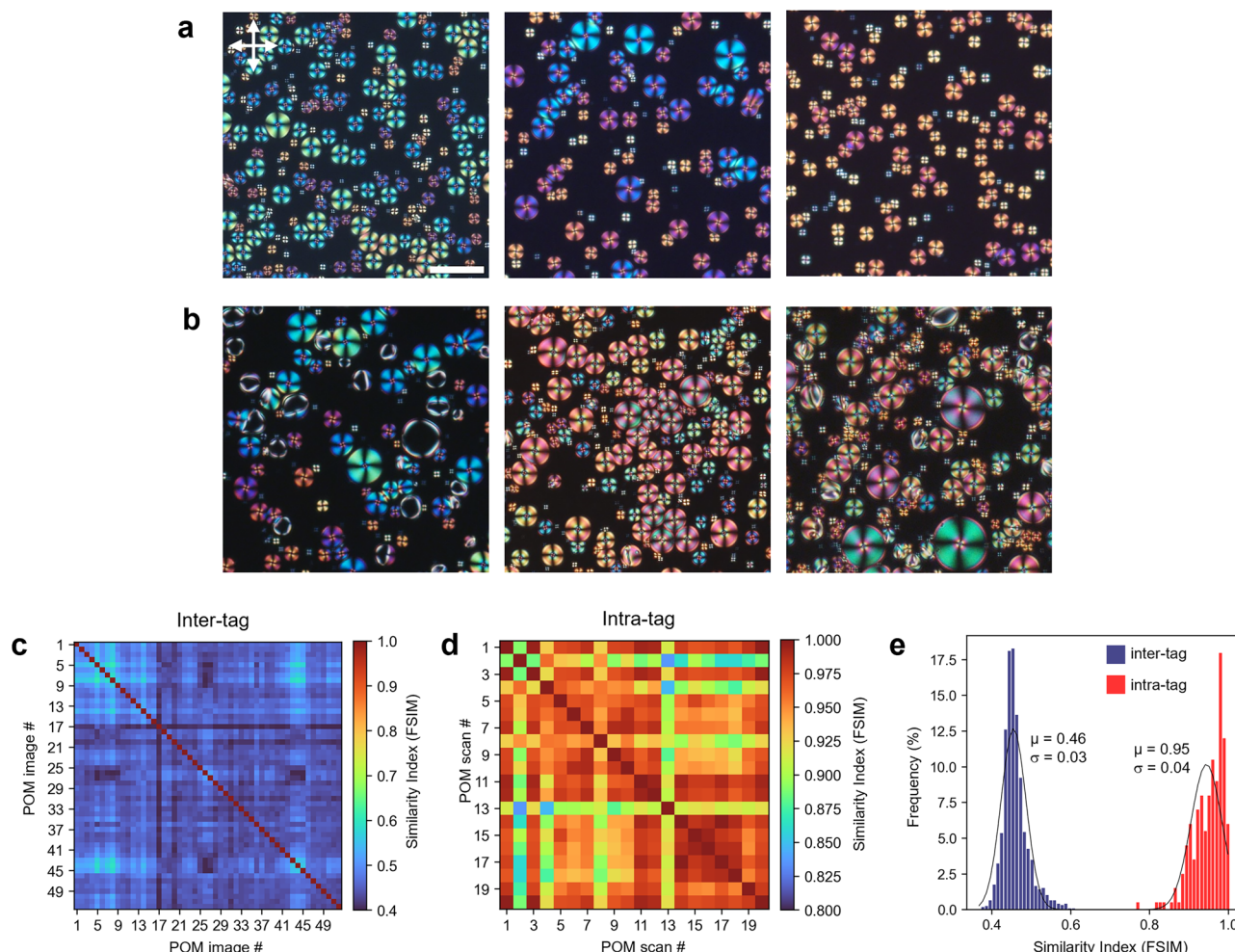


Fig. 6 | C12 films' potential as physically unclonable (PUF) tags. a, b Example of the variability found in C12 films from the same production batch (a) and from different production batches (b) observed by POM. Scale bar represents 50 μm . **c** Inter-tag similarity matrix, representing the FSIM values obtained for POM images of 52 distinct C12 tags (11 batches produced in a time frame of 3 years, 1–9 tags per batch). Each matrix element represents the similarity (FSIM index) between 2 POM images. The diagonal elements represent the FSIM index for the same tag images,

and the non-diagonal elements represent the FSIM index for pairs of different tags. **d** Intra-tag similarity matrix, representing the FSIM values for 20 POM images of the same C12 tag obtained on different days and under different conditions (Illumination, focus, contrast, translation and rotation). **e** Distribution histograms of the inter-tag and intra-tag FSIM values from (c, d), superimposed with Gaussian distributions with mean and standard deviation equal to those of the inter- and intra-tag FSIM values.

When compared with the films prepared with C_8mimCl and the C12 molar composition, C12 presents the advantage of having thermal memory, i.e. allowing the identification of the past exposure of the film to temperatures higher than 35.6 $^{\circ}\text{C}$ due to the irreversibility of the optical texture pattern upon heating and subsequent cooling to room temperature (Supplementary Fig. S11).

For the stated reasons, the C12 formulation is considered the most promising to prepare PUF tags and C12 films are further studied in the following sections.

C12 films as PUF authentication tags

To check the authenticity of an object in PUF tag systems, the physical tag on the object is challenged and responds to the challenge with a unique fingerprint pattern that serves as authentication code or key for the tagged object¹ (Fig. 1e). In this work, the physical tag is envisaged as a small millimetre-size label composed of a C12 film (the C12 tag), which could be either applied directly on the object or on an independent substrate for subsequent attachment to the object (Fig. 1a). We envisage also an AI-based authentication system pre-trained with a large number of C12 PUF tags. For authenticity checking, the tag is challenged by photographing it with an optical microscope, generating as a response a POM image and/or a BF

image. Then, the microscopy images are analysed by the AI-based authentication system to determine if they correspond to the fingerprint of an authentic tag. This is the first authentication level of the tag. The gas-responsive properties of LC droplets^{17,44,45} can be used to implement a second authentication level (Fig. 1e).

The security of a PUF tag system can be evaluated by the number of possible unique responses or fingerprints that it can exhibit, also known as the Encoding Capacity (EC)¹. In C12 films, the large intra- and inter-batch variability of optical patterns created by LC droplets in POM images (Fig. 6a, b) suggests that a large number of unique tags can be created.

Considering just the first level of authentication with POM images, the EC can be estimated as l^m according to the number of pixels (m) of the image and the number of possible colours for each pixel (l)¹. Taking into account that only approximately 1% of the pixels would contribute to the EC because most of the POM image is black, we can estimate $\text{EC} = 256^{28,000}$ ($\sim 10^{56,000}$), which is largely above the EC reported for emergent PUF systems based on engineered sustainable materials ($\text{EC} = 10^{18}$, 10^{30})^{46,47} and for PUFs based on LC materials ($\text{EC} = 10^{55}$, 10^{280})^{13,14}, and practically infinite. Thus, it would be impossible to produce two C12 tags with the same POM optical pattern. Furthermore, considering the possibility of having in our system additional authentication levels represented by (i) the BF image and (ii) the gas-

induced optical texture change pattern, we can see this estimate as the minimum expected EC for the C12 tags.

Most PUF systems based on images of optical patterns convert the images into a binary code that is used for authentication instead of the image itself^{10,14,46–48}. While this process is still the standard and may simplify the authentication process, it limits the EC of the PUFs. For our proposed PUFs, we envisage an AI authentication process based on deep-learning image identification, which is directly applied to the microscope images to take full advantage of the images' richness (namely in colours, and diverse optical textures), maximise the EC and robustly cope with artefacts and noise in image acquisition during the authentication process. In a real-case scenario, where the user could use an adapted smartphone to authenticate the tag, artefacts such as different magnification, rotation, brightness, shifts, focusing and mixtures of these parameters would be frequent. AI-authentication systems are known for their outstanding ability to learn and recognise the characteristics of authentic PUF patterns, even in the presence of such artefacts and noise^{5,11}. The authentication pipeline for the C12 tags is envisaged for future work. We expect that only a few seconds are required to authenticate a film with a previously trained AI authenticator, based on similar systems reported in the literature^{5,11} and our previous work on AI-classification of volatiles using similar optical textures¹⁸.

C12 tags PUF performance characterisation

The potential of C12 films as tagging materials for PUF systems can be further characterised using standard PUF performance metrics⁴⁹ such as uniqueness, robustness and reliability. In many PUF authentication systems that use tag images, there is an initial step of image binarisation, as mentioned before. The Hamming Distance is commonly employed as a similarity measure between binary images to calculate the PUF performance metrics, namely, in some reported LC-based PUFs^{13–15}. We intend to implement an AI-authentication algorithm that analyses the RGB images of the tags without binarisation, thus the Hamming distance is not applicable. We employed the FSIM⁴³ as an alternative image similarity measure that is adequate for RGB images and was previously reported for AI PUF authentication¹¹. To prevent image similarity underestimation due to artefacts caused by sample positioning on the microscope stage (e.g. rotations, shifts), the images were previously aligned with a registration algorithm (TrakEM2⁵⁰ macro in FIJI⁵¹). The uniqueness, robustness and reliability of the proposed PUF system were then studied for the aligned images.

To verify the uniqueness, we calculated the FSIM between the microscope images (POM or BF) of 52 independent C12 tags (inter-tag similarity). The inter-tag POM similarity matrix in Fig. 6c represents the FSIMs calculated for the POM images of 1352 possible tag pairs ($(52 \times 52)/2$). It shows a typical diagonal feature, meaning that a high optical pattern similarity only exists for the same tag. An average inter-tag similarity of 0.46 ± 0.03 (46%) was obtained, which is close to the ideal value of 0.5 for well-performing PUF tags¹⁰. This demonstrates that all tags are different from each other and that each C12 tag generates a unique POM optical pattern. The uniqueness and unclonable character of C12 tags is due to the unpredictability and randomness of the optical patterns, which are inherent to the non-deterministic tag production process. This ensures that replicating the tag optical pattern is impossible, even by the manufacturer.

The robustness criterion of PUF tags is also verified by C12 tags, especially for the POM images, as shown by the intra-tag similarity matrix (Fig. 6d), which represents the FSIMs calculated for 20 POM images of the same C12 tag acquired under different environmental and operational conditions (e.g. different days, contrast, brightness and rotation). The goal here was to mimic conditions that could occur in reality, during a tag authentication process. The high FSIM index obtained for every pair of POM images of the same tag led to an average intra-tag similarity of 0.95 ± 0.04 (95%), close to the ideal value of 1 (or 100%)¹⁰, which indicates that the C12 tag system is robust, i.e. regardless of the image acquisition conditions, the optical pattern of the tag is correctly captured and thus the tag would be correctly identified by a potential authentication system.

An ideal authentication performance has zero false negative and false positive rates (FPRs). The FPR is the probability that one tag is incorrectly recognised as another tag (or that a fake tag is recognised as genuine). The false negative rate (FNR) is the probability that a genuine tag is incorrectly recognised as fake^{52,53}. To estimate the threshold required for authentication with our proposed system, the histograms of the intra-tag and inter-tag similarity for POM images (Fig. 6e) were fitted to a Gaussian distribution and the threshold for true authentication was determined as the intersection between the two Gaussian distributions ($\text{Threshold}_{\text{FSIM}} = 0.67$). The corresponding FPR and FNR^{52,53} are in the order of 10^{-12} , suggesting that a PUF authentication system based on the C12 films and their POM images will have a performance close to ideal, with very low erroneous tag recognition rates.

Regarding the BF images, a larger overlap of the BF intra and inter-tag similarity distribution histograms was obtained (Supplementary Fig. S12), pointing to a less robust authentication system than the POM-based system at its present form. In the future, the similarity analysis of the BF images of the tag could be optimised, as in the present analysis, the image brightness and contrast differences contributed to decreasing the FSIM index.

Finally, it is important to note that a PUF tag must be reliable, i.e. it must yield the same response every time, even after numerous uses and long periods of time. Our long-term morphological stability study of C12 films (Fig. 5) showed that they maintain the droplet positions and LC configuration at least for 2 years, corresponding to a FSIM index for POM images of $94 \pm 3\%$. This similarity is within the range of the intra-tag FSIM values for POM images ($95 \pm 4\%$, Fig. 6e), indicating that the C12 films are reliable as PUF tags, because they yield practically the same response over 2 years.

Dynamic VOC-response of C12 tags as a second PUF authentication level

The diffusion of analytes as volatile organic compounds (VOCs) through 5CB droplets embedded in gelatin ionogels decreases the LC molecular order and can trigger a phase transition from nematic to isotropic, similar to impurity- or thermally-induced orientational transitions^{17–20,22,24,25,44}. C12 films also exhibit this VOC-responsive feature. We observed that flushing vapours of low-toxicity organic solvents such as acetic acid (Fig. 7a) or acetone (Fig. 7b) leads to the fast (less than 10 s) loss of LC order within the droplets with their optical texture shrinking, until complete isotropisation. Here, in both cases, the initial POM field of view before exposure reveals a radial droplet population. When ambient air is flushed to the films, the LC molecules reorganise themselves (in less than 30 s), albeit most of them adopting an axial droplet profile (Fig. 7a, b, at 15 s). During successive exposure/recovery cycles, the droplets recover their axial structure after isotropisation, revealing that in C12 films, axial droplets are probably a more stable formation than radial ones. It is possible that the relatively long and quite flexible alkyl chain of C₁₂mimCl offers sufficiently weak anchoring that renders any initial radial droplet formation a metastable structure, when compared to the more stable axial organisation, favoured under weak anchoring conditions. Finally, the optical response of C12 tags to organic vapour and air can be recorded either as a POM video (Fig. 7) or as a one-dimensional signal corresponding to the variation of light intensity transmitted through the tag when positioned between two crossed polarisers^{17,19,20,22} (Supplementary Fig. S13a).

The C12 tag's response to the organic vapour challenge (either as a POM video or as a one-dimensional signal) is a dynamic optical pattern that can serve as a second level of authentication. A dedicated AI algorithm pre-trained to recognise this pattern would serve as the basis for the authenticity verification. This is supported by our preliminary work on VOC identification by machine learning, which showed that after training a VOC classification model with 12 distinct VOCs, acetic acid got a high correct classification rate (Supplementary Fig. S13b, c).

The second authentication level further enhances the security of C12 PUF tags because it reduces the likelihood of counterfeiting tagged products.

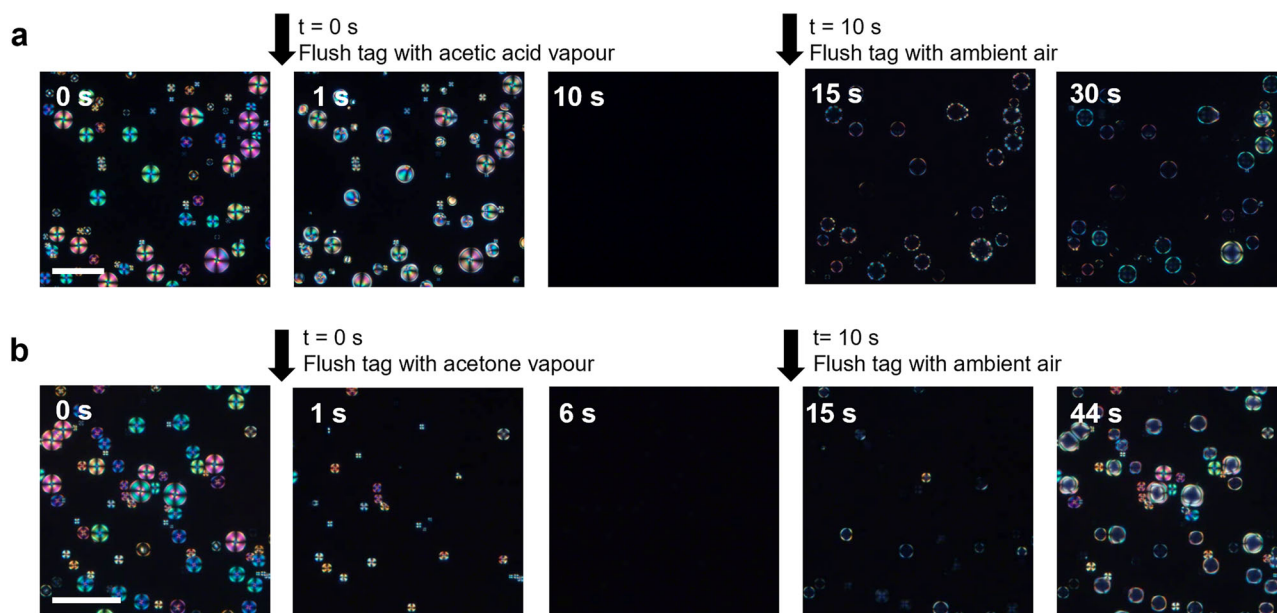


Fig. 7 | POM images showing typical patterns of optical changes in C12 tags when challenged with vapours of VOC, followed by ambient air. Acetic acid (a) and acetone (b) were used as model VOCs to show that a saturated atmosphere with VOC causes the gradual disorganisation of the radial LC droplets until

isotropisation. Subsequent exposure to air promotes the LC re-organisation into the axial LC droplet configuration, generating typical optical fingerprint patterns. Scale bar corresponds to 100 μm .

In this case, the tagged product or object would only be validated as authentic if the tag would pass 2 test levels: (i) its static POM optical pattern should be identified as authentic by a pre-trained automatic image recognition model; and (ii) its dynamic POM optical response when challenged with a low toxicity organic vapour should be recognised as the typical response of C12 tags to that vapour (Fig. 1e). Thus, in the unlikely event of copying or faking the optical pattern of a C12 tag, despite the fake tag passing the first level of authentication, it would not pass the second level because it would lack the dynamic optical response pattern when challenged with organic vapour and air.

C12 tags processing versatility

C12 optical ionogels are easily processed in different ways to produce tags with distinct formats, namely films or moulded with different three-dimensional shapes (Fig. 8). Films can be prepared by using an automatic film applicator equipment to spread the ionogel onto planar, flat or patterned, rigid or flexible substrates (e.g. glass, cellulose acetate sheet, Fig. 8a–c), but also by brushing the ionogel as an ink over the substrates or objects (Fig. 8d, e). As the C12 films are translucent when spread onto surfaces, the PUF tags will be invisible to the naked eye, hidden or “merged” with the object, and their unique optical patterns are only detectable by POM microscopy. In addition, the C12 formulation consists of 80% bio-based and biodegradable components (gelatin and water), representing an example of a sustainable and simple material to tackle the complex needs of the authentication and anti-counterfeiting field.

Anti-tamper and temperature-control features of C12 tags

Tampering refers to any attempt at package corruption or unauthorised opening of the package and is a global concern in many businesses because it is associated with product stealing and/or their replacement by fakes or counterfeits. To protect themselves from such threats, manufacturers often have anti-tamper or tamper-evident labels sealing the packages of their products. C12 tags can be enriched with the possibility of detecting tampering attempts as they irreversibly lose the typical POM pattern of LC droplets if subjected to mechanical abrasion (e.g. finger-pressing) or detached from an object (Fig. 9). Such changes in the tag’s POM pattern corresponds to a similarity of 89% and 93% (FSIM = 0.89 and 0.93),

respectively, in relation to the original patterns, which are slightly lower values than the average intra-tag FSIM values for POM images of a same tag (95%, Fig. 6e). This feature has the potential to be used as tampering evidence, to detect potential attempts of unauthorised touch, adulteration, or tag removal from the tagged object. In addition, C12 tags have temperature-sensitivity properties due to the thermotropic nature of the LC 5CB. In bulk material, the orientation of 5CB molecules varies with temperature from ordered (in solid state, at $T < 22.5^\circ\text{C}$) to totally disordered (in liquid, isotropic state, at $T > 35^\circ\text{C}$)⁵⁴. At intermediate temperatures, in the nematic phase, 5CB rod-like molecules exhibit orientational order of the long molecular axis and are birefringent, i.e. they can change the plane of incident polarised light, appearing as bright optical textures under POM⁵⁵. Increasing temperature triggers molecular orientational transitions, which under POM are identified as changes of colour and, eventually, isotropisation, if the temperature is higher than 35°C . Thus, 5CB-based materials, as the C12 tags, are inherently thermo-sensitive.

Our thermal investigation of C12 tags (Fig. 10 and Supplementary Fig. S11) showed that the radial (and twisted radial) droplet configuration is metastable and irreversible, as upon heating the films until LC isotropisation (35.6°C , Fig. 10a) and subsequently cooling them to room temperature (23°C , Fig. 10a), the LC droplets do not recover the radial configuration, adopting instead the axial configuration. The axial configuration, however, is reversible, which was confirmed when the reconfigured C12 film was subjected to a second heat/cool cycle and the axial configuration was totally recovered (Supplementary Fig. S14a, b)^{22,56}. These observations are in line with our VOC investigations, and as we have already mentioned previously, analyte-induced transitions share characteristics with thermally-induced transitions^{22,56}.

This interesting reconfigurable-texture capability of C12 films can be proven advantageous and utilised as a method for temperature monitoring of objects tagged with C12 PUF tags. Since the axial texture is only present if the tag is heated and cooled (as the original radial texture is not recovered), it is possible to detect whether the object was exposed to high temperatures. This feature could be useful for tracking the transportation and storage of thermo-sensitive products that require room temperature conditions and cannot sustain temperatures higher than 35.6°C . In this case, the C12 PUF

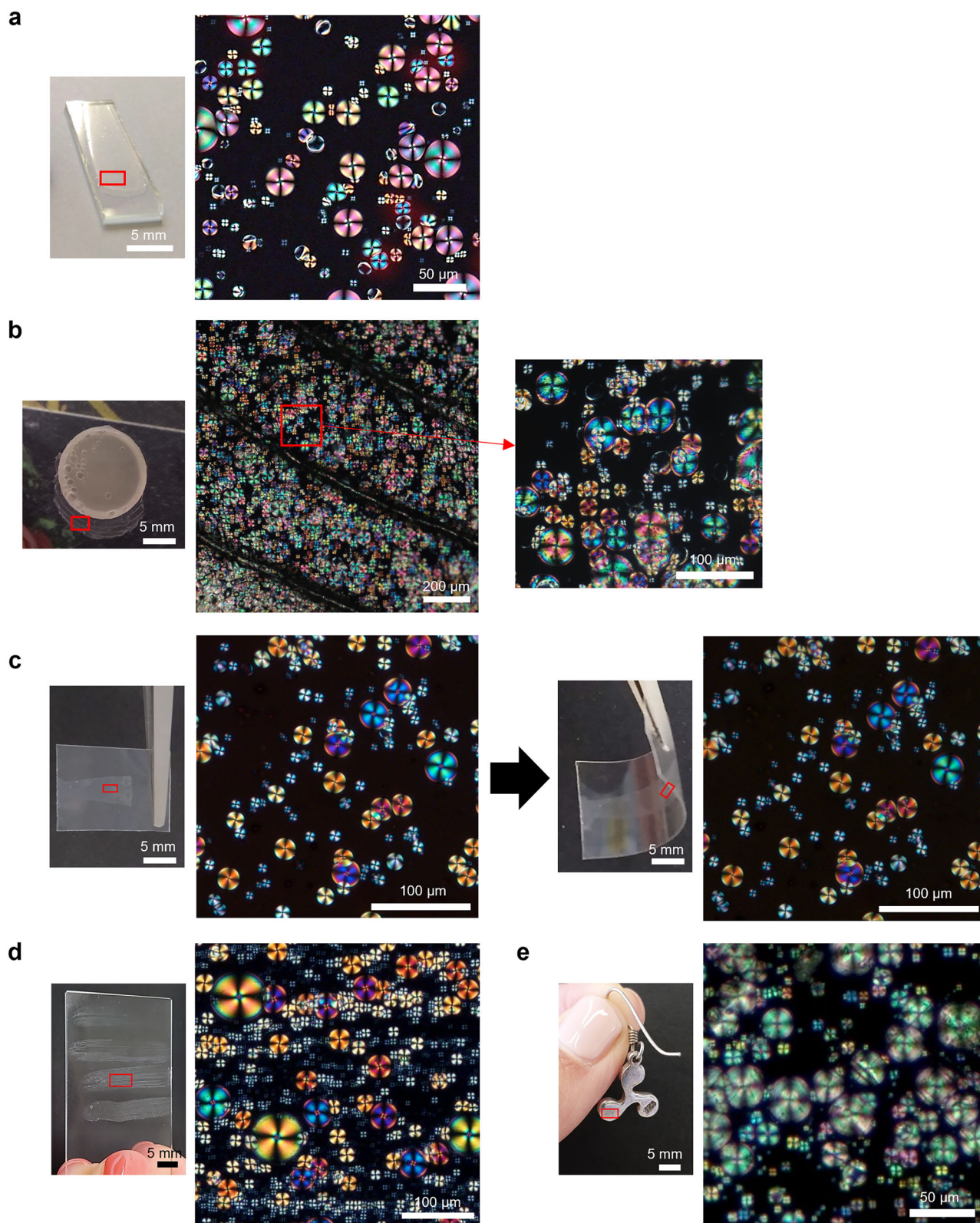


Fig. 8 | C12 optical ionogel processing versatility and respective POM images.
a Deposition with a film applicator onto a glass slide. **b** Moulding using a disc template with a patterned, flat, thin surface. **c** Deposition with a film applicator onto

a flexible cellulose acetate sheet, showing identical POM images before and after bending. **d** Brushing as an ink onto a glass surface. **e** Brushing ink onto the surface of an earring.

tag would have the double function of authentication and temperature control.

The reconfigured axial droplet pattern of C12 films has long-term stability of at least 2 years (Supplementary Fig. S14c, d), and the

reconfiguration is a simple and mild thermal process. As such, it can also be considered a method to generate a new family of PUF tags.

To estimate the potential of the reconfigured family of PUF tags, we calculated their metrics. The FSIM matrices for inter-tag and intra-tag

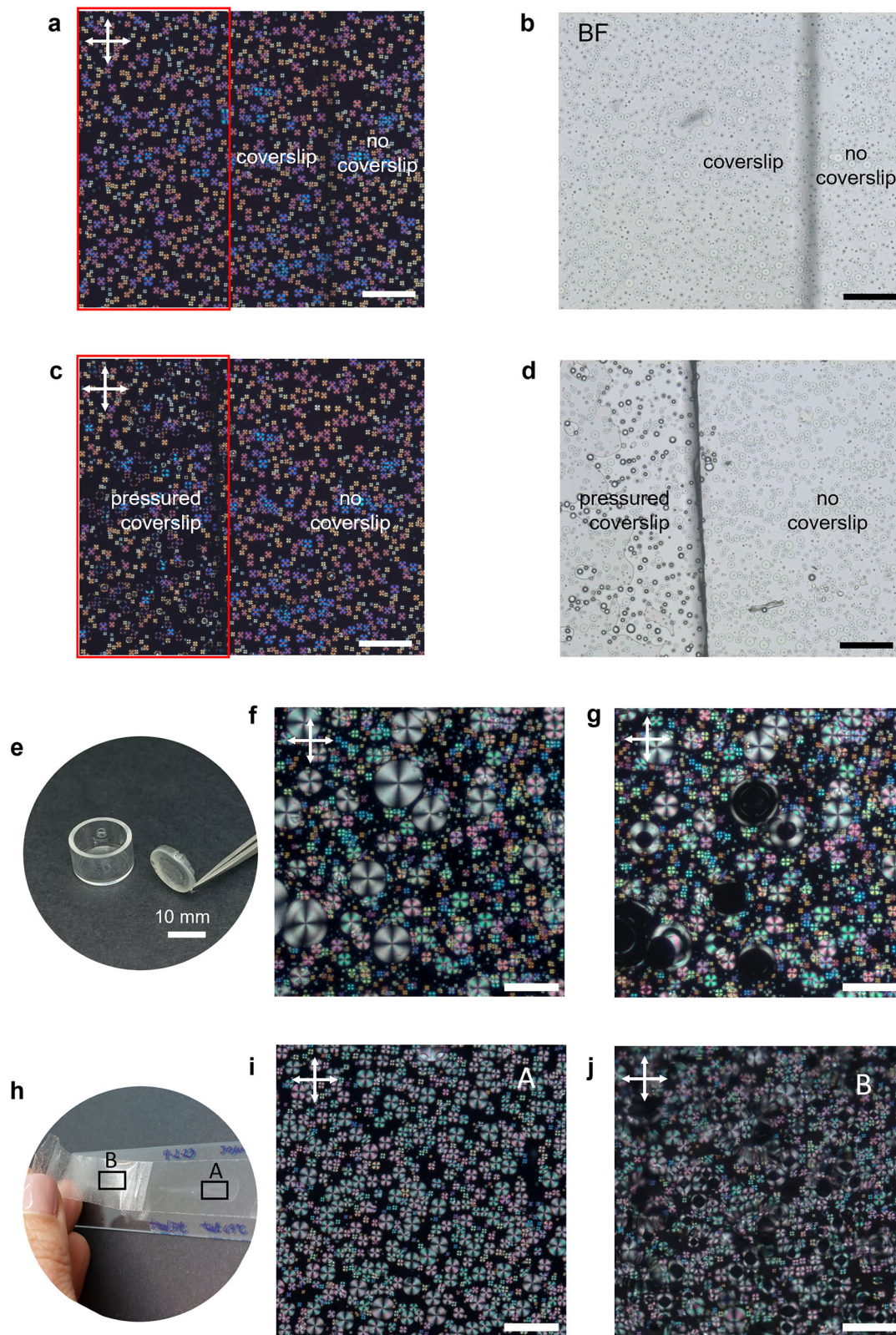


Fig. 9 | Tamper-evidence property of C12 films. **a** POM and **b** BF image of a C12 film spread on a glass slide and covered with a coverslip. The droplets are not affected by the weight of the coverslip. **c** POM and **d** BF image after finger-pressure was applied on the coverslip. The droplets underneath the pressured area (red rectangle) mostly change to the axial configuration. **e** C12 moulded using the bottom of a glass vial as the mould. **f** POM image obtained by imaging the bottom of the vial before

detaching the moulded film. **g** POM image obtained from the detached moulded film. **h** Macroscopic aspect of a C12 film spread on a regular office tape glued to the glass slide. **i** POM image of the film in an untouched region of the tape (A region in **h**). **j** POM image of the film in a region of the tape that was detached from the glass (region B in **h**). Scale bar represents 100 μm .

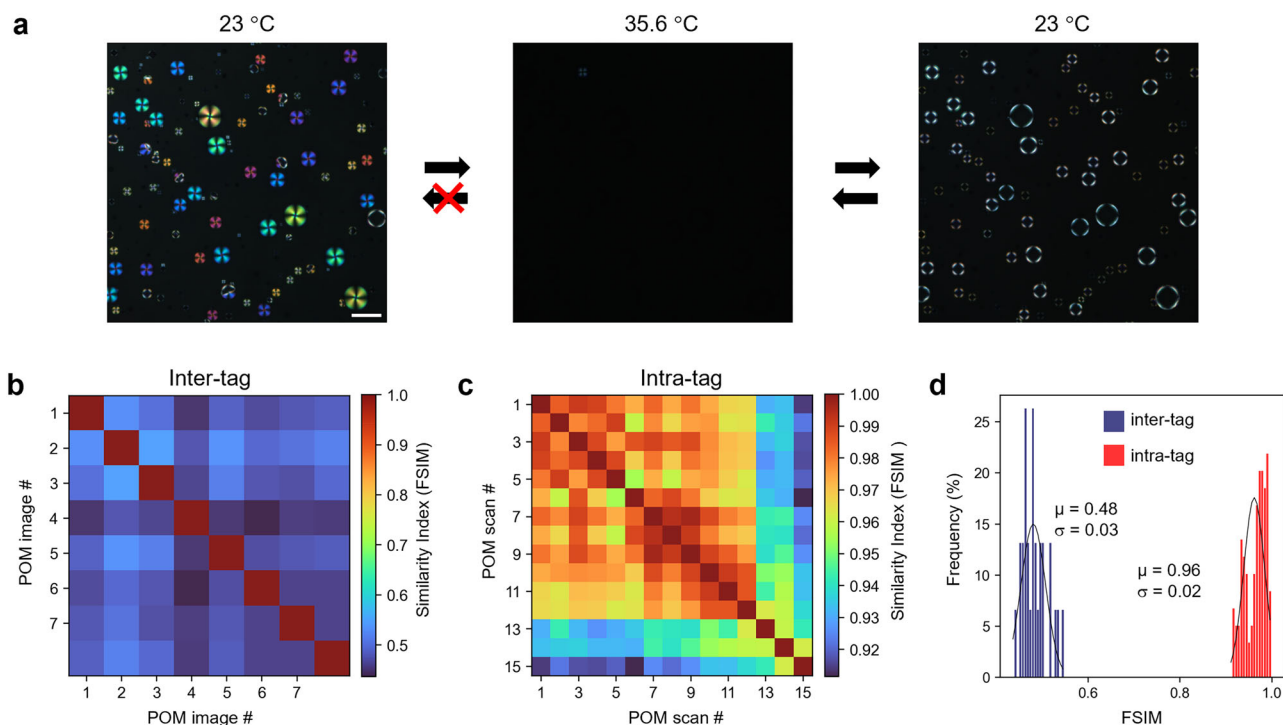


Fig. 10 | Thermal reconfiguration of C12 tag and assessment of the respective PUF performance. **a** POM images showing the irreversible effect of subjecting a C12 film to a thermal treatment consisting of heating and cooling down to obtain reconfigured tags with the droplets in axial configuration. The scalebar represents 50 μm . **c** Inter-tag similarity matrix was calculated for POM images of 8 thermally treated C12 tags from the same batch of production. Each matrix element represents the similarity (FSIM index) between 2 POM images. The diagonal elements

represent the FSIM index for the same tag images, and the non-diagonal elements represent the FSIM index for pairs of different tags. **d** Intra-tag similarity matrix, representing the FSIM indexes for pairs of POM images of the same C12 tag taken in different conditions (different days, illumination, focus, contrast, translation and rotation). **e** Distribution histograms of the inter-tag and intra-tag FSIM values from (b, c), superimposed with Gaussian distributions with mean and standard deviation equal to those of the inter- and intra-tag FSIM values.

similarity of POM images of eight C12 axial tags from the same production batch allowed us to verify the uniqueness (inter-tag FSIM = 0.48 ± 0.03) and robustness (intra-tag FSIM = 0.96 ± 0.02) parameters required for PUF tags, with a clear separation between the intra and inter-tag FSIM distribution histograms (Fig. 10c–e). Like the native radial C12 tags, the FSIM distribution histograms of BF images showed a slight superimposition (Supplementary Fig. S15), confirming the better suitability of POM than BF microscopy images for the PUF tags.

Discussion

Optical ionogel formulations using gelatin as matrix, an imidazolium chloride IL as solvent and stabiliser, and the LC 5CB as optical probe have been studied as potential PUF tags. These unique materials take advantage of the cooperative self-assembly and dynamic properties of each component, introducing a competitive approach for polymer-dispersed liquid crystal (PDLC) materials in security applications. Here, the IL has a crucial role in the stability of the materials, in the design of the optical patterns of the tag and dynamic response to organic vapours¹⁷.

The gel formulation with $\text{C}_{12}\text{mimCl}$ IL (C12), with an 80% biodegradable formulation, was stable for up to 4 years and the most mechanically robust, thus it was investigated as a taggant material. The random distribution of LC droplets in films of C12 gel yields subtle tags that are invisible to the naked eye and present high EC. The droplet contours are visible under BF optical microscopy, but the coloured and unique optical textures created by the LC are only revealed using POM—these textures or patterns are used as the fingerprint for the first level of authentication of the tag. Additional security features can be implemented using the stimuli-responsive nature of 5CB droplets, namely (i) a second level of authentication, based on the droplets typical optical response to vapours of low toxicity solvents, as acetic acid or acetone, (ii) a temperature exposure control feature, based on the irreversible temperature-driven reconfiguration of the LC droplet

configuration, and (iii) a tamper-evidence feature, based on the irreversible changes of the ionogel matrix and LC optical textures if the tag is subjected to physical abrasion.

The formulation C12 represents an interesting platform technology to design cost-effective and sustainable PUF tags with the required essential characteristics, including long-term stability, uniqueness, mechanical robustness, and high EC. Tags made with C12 films offer an 80% biodegradable approach to anti-counterfeiting, presenting 2-level security, temperature monitoring and tamper-evidence protection. The fabrication methods are simple, mild and scalable. Namely, at laboratory scale, the C12 optical ionogel is prepared in 30 min at room conditions, and standard film applicator equipment can spread an A3 sheet-sized surface in less than 5 min, which corresponds to 100,000 tags with 1 mm^2 per A3 sheet. This results in low-cost tags (estimated material cost of the C12 film: 0.007 €cents/tag with 1 mm^2 area each) with potential for markets where products are handled at room temperatures (18–34 $^{\circ}\text{C}$), spanning diverse industries, including packaging of pharmaceuticals, personal care, cosmetics, and electronics. We are aware of the limited biocompatibility of the LC 5CB. It is, thus, important to note that to increase the safety of the tag, a protective matrix or layer can be added to further block the 5CB inside the tag and prevent its contact with the users' bodies.

Regarding the authentication hardware, at the laboratory scale, we used a polarised light benchtop microscope to record the tags' static optical textures and dynamic optical responses. While it is convenient in the laboratory, for practical applications, it should be replaced by a portable, hand-held and simple device. Future work could explore the integration of miniaturised POM hardware and image recognition in a more user-friendly platform, namely, a smartphone-based tool. In a real-world scenario, shifts, rotations, illumination and focusing differences during capture of the tag image are expected to happen. An authentication pipeline based on image recognition with AI is a robust and safe option that could

overcome potential issues caused by artefacts derived from image acquisition.

To conclude, the C12 optical ionogel is versatile on its own due to the ease of processing in different formats. In this work, we explored the film format, but other formats can be envisaged, such as fibres or bioinks for 3D-printed structures, easily adaptable to the needs. Taken together, the long-term stability and mechanical robustness of the films, their performance as PUFs, the processing versatility, and the unique biobased composition of C12 optical ionogel represent a promising and innovative solution for high security authentication and anti-counterfeiting, compatible with the recent Digital Product Passport and Ecodesign for Sustainable Products regulation, contributing to a Future of responsible and environmentally sustainable consumption patterns.

Methods

Preparation of biobased optical ionogels

The biobased materials C2, C4, C6, C8, C10 and C12 were produced by preparing, in a glass vial at 37 °C under magnetic stirring, viscous emulsions containing the four components of the material (gelatin, IL, LC and deionised water—quantities shown in Supplementary Fig. S2c), based on the protocol described in the work of Hussain et al.¹⁷ with adjustments made depending on the IL used (see detailed experimental procedure in the Supplementary Information). The viscous emulsions were left to gelate at least overnight, and the gel formation was confirmed by the glass vial inversion test.

The biobased materials C2_a and C8_a, with C12 molar composition but different ILs, we prepared as the C12 biobased materials, by replacing the IL with C₂mimCl and C₈mimCl, respectively, and using the C12 molar composition (Fig. S2a).

The ionogel and hydrogel controls were prepared according to the same experimental procedure, but replacing water with the LC component (in ionogels) or the LC and the IL components (in the hydrogel). The detailed experimental procedure and quantities of each component in the controls are found in Supplementary Fig. S2d

Preparation of biobased optical ionogel films

To prepare films, 5–10 µL of C2, C4, C6, C8, C10 or C12 viscous solutions was deposited, while still warm, onto a glass slide previously cleaned with ethanol, and spread as films using an automatic film applicator (TQC Sheen, Netherlands) with a heated bed (at 37 °C) and a quadruplex accessory sliding at 50 mm/s, with a pre-defined spacing of 30 µm to the heated bed. The films were left at room conditions ($T = 22 \pm 1$ °C and relative humidity of RH = $53 \pm 2\%$) for 24 h before characterisation, unless otherwise stated.

Air-stability assessment of C2, C8 and C12 biobased optical ionogels

C2, C8 and C12 optical ionogel formulations and gelatin hydrogel controls were prepared in a glass vial. Approximately 400 µL per sample was transferred to an O-ring mould (10 mm inner diameter; 3 mm height) fixed on top of a glass slide, to generate a disk-shaped gel, and left at room conditions for 30 days (temperature of $T = 22 \pm 1$ °C and relative humidity of RH = $53 \pm 2\%$), during which the samples' weight was monitored. The relative weight variation of the samples on each day (Δweight) was calculated using as a reference the weight on day 0:

$$\Delta\text{weight} = \frac{\text{weight} - \text{weight}_{\text{day0}}}{\text{weight}_{\text{day0}}} \times 100\%$$

Duplicates of each formulation were analysed, and the results were plotted as the average and standard deviation of the duplicates' measurements.

Photographs of the gel discs were taken at the initial and final time points of the experiment.

Mechanical and structural characterisation of the biobased optical ionogels

Rheometry. The viscoelastic properties were studied using a rheometer (MCR 102, Anton Paar, Austria) with the temperature controlled at 20 °C. Samples of C2, C8 and C12 and of the gelatin hydrogel control were prepared in a glass vial. Approximately 400 µL per sample was transferred to an O-ring mould (10 mm inner diameter; 3 mm height) placed on top of a glass slide covered with parafilm and left to gelate overnight at approximately 50% relative humidity and 21 °C. To analyse these samples, after overnight gelation, they were transferred from the O-ring to the measuring accessory of the rheometer (parallel sandblasted plate PP08/SP). Since the C4 and C6 formulations are viscous solutions, these samples were dispensed (approximately 250 µL) with a pipette directly from the preparation glass vial to the rheometer, more specifically to a measuring plate cone CP25-2. An amplitude sweep (or strain sweep) was performed (strain varied from 10^{-5} to 1 at 10 rad/s) to choose a strain at the linear viscoelastic regime, where no variation of G' and G'' is observed, to perform the frequency sweeps. A strain of 0.05 was chosen for C2, C8 and C12 samples, and a strain of 0.2 was chosen for C4 and C6 samples. Frequency sweep measurements were then performed in the angular frequency range of 0.06–12 rad/s, with a strain of 0.05 or 0.2. Extra samples of C12 optical ionogel were left in the o-ring mould for 1 month at room conditions (22 ± 1 °C and $52 \pm 3\%$ RH) and analysed in amplitude and frequency sweeps as explained above. The frequency sweeps were performed with a strain of 0.00005, in the linear viscoelastic region, as determined by the amplitude sweep measurements. Duplicates of each formulation were measured, and the results were represented as the average and standard deviation of the measurements made for the duplicates.

X-ray scattering. X-ray scattering images of C2, C8 and C12 optical ionogels, and respective gelatin hydrogel controls were obtained using a sealed tube microfocus CuK α diffractometer (D8 Venture, Bruker AXS, Germany) coupled to a CMOS detector (Photon100, Bruker AXS, Germany), operated at 50 kV and 1 mA. C2, C8 and C12 formulations were prepared in a glass vial and left to gelate overnight at approximately 50% RH and 21 °C. To obtain the scattering images, a sample of the optical ionogel was cut with a knife and transferred to the diffractometer loop support, where the measurements were performed. The sample-to-detector distance was 60 mm, and X-ray scattering images were produced without oscillation, with a 10 s exposure time. All measurements were performed at room temperature (20 °C).

Raman microscopy. 2D Raman maps of the surface of axial and radial droplets in C12 films were obtained using a Confocal Raman Microscope (ALPHA RAS 300, OXFORD Instruments WITec, Germany) with a 532-nm argon laser at 0.5 mW of power.

Morphological characterisation of biobased optical films

POM and BF microscopy. The films were observed using an Axio Observer Z1/7 optical microscope (Zeiss, Germany) coupled with an Axiocam 503 colour camera (Zeiss, Germany) and equipped with the ZEN 2.3—ZEN Pro software (Zeiss, Germany) for microscope control, image acquisition and processing. POM images were acquired with the samples placed between crossed (90°) polarisers. BF images were acquired without using the polarisers.

Droplet size distribution analysis. The LC droplets' diameters were determined using a custom-made Python image processing script. The Hough Gradient Method function (HoughCircles()) from Python's library OpenCV was employed for detecting circles in BF images of the films and measuring their diameter. Diameters were measured for a minimum of 400 droplets detected in, at least, 8 different regions of interest (ROI) of BF images of at least 2 independent films (C2: 2 films, 8 ROIs, 1699 droplets; C4: 4 films, 6 ROIs, 1143 droplets; C6: 3 films, 4 ROIs, 2037 droplets; C8: 3 films, 9 ROIs, 1323 droplets; C10: 3 films, 7

ROIs, 436 droplets; C12: 7 films, 9 ROIs; 2440 droplets). The diameters were represented in histogram plots, and the diameter average and standard deviation were calculated over the droplet population measured for each formulation. The Polydispersity Index (PDI) was calculated as the ratio between the standard deviation and the average of the diameter.

Atomic force microscopy (AFM). AFM analysis was performed on the surface of C2, C8 and C12 films using an Asylum Research MFP-3D Stand Alone AFM system operated in alternate contact (tapping) mode. The imaged LC droplets in each sample were selected among those with the most frequent diameter in each sample. Measurements were done with two commercially available silicon AFM probes: Olympus AC160TS ($k = 26$ N/m; $f_0 = 300$ kHz) and Olympus AC240TS ($k = 2$ N/m; $f_0 = 70$ kHz) for operation in air and in liquid media, respectively. The resulting topographs were plane-fitted, and the data were analysed using Gwyddion software.

Stability during storage at room conditions. Using the POM, a representative ROI of the C12 film was selected. BF and POM images were taken periodically on the selected ROI over a period of 4 years. The film was stored at room conditions ($RH = 54 \pm 11.3\%$; $T = 22 \pm 1.4^\circ\text{C}$) during the period of this study. The resulting set of BF and POM images was aligned using the TrackEM2⁵⁰ plugin from Fiji Software⁵¹ and then cropped to select only the area that was common to all aligned images. The aligned and cropped images were then processed with a custom-made Python script to calculate the pairwise similarity of the images taken over time and represent the calculated similarity values in a 2D matrix (similarity matrix). The feature similarity index (FSIM) algorithm⁴³, as implemented in the PyTorch Image Quality Python library (PIQ, version piq 0.8.0)⁵⁷, was used to calculate the pairwise similarity of the images.

Calculation of C12 film PUF tag performance metrics

In this work, we defined “PUF tag” as one region of a C12 film with the area of the film micrograph taken at $10\times$ magnification ($0.87\text{ mm} \times 0.77\text{ mm} = 0.67\text{ mm}^2$).

Uniqueness. A PUF tag must be distinguishable from every other PUF prepared with the same manufacturing method. For that, the PUF response should be different by 50%¹⁰ (or similar by 50%) from other PUFs’ responses.

The FSIM algorithm was used to calculate the pairwise similarity between POM images from 52 independent C12 films (denoted as “inter-tag FSIM” or “inter-tag similarity”). The 52 films were from 11 different production batches (1–9 films per batch). The obtained FSIM indexes (values between 0 and 1, equivalent to 0% and 100% similarity, respectively) were represented in a 2D matrix where each cell represents the similarity between a pair of POM images from different films. For visualisation purposes, the similarity matrix’s cells were coloured according to a colour scale matching the FSIM values’ scale. The average inter-tag FSIM was used as a metric for uniqueness. This permitted us to assess if the POM patterns of the films were sufficiently different from each other (i.e. inter-tag FSIM ≈ 0.5) for the C12 tags to be considered unique.

The same procedure was followed for BF photos of the C12 tags.

Robustness. A PUF tag must yield the same response under varying acquisition conditions (such as different environmental conditions or operational conditions), meaning that the responses of the same PUF tag in different conditions should be close to 100% similar. To assess the robustness of the C12 tags, the FSIM algorithm was used to calculate the pairwise similarity between 20 POM images of the same C12 film (denoted as “intra-tag FSIM” or “intra-tag similarity”) acquired in different days (over 19 days with $RH = 56.5 \pm 6.7\%$ and $T = 21.3 \pm 0.4^\circ\text{C}$), with varying (randomly selected) microscope brightness, contrast and sample rotations. The obtained FSIM indexes (values between 0 and 1,

equivalent to 0% and 100% similarity) were represented in a 2D matrix (the intra-tag similarity matrix), as explained above. The average intra-tag FSIM was used as a metric for robustness. This permitted us to assess if the POM pattern of the C12 film is sufficiently identical under different acquisition conditions (i.e. intra-tag FSIM ≈ 1.0).

The same procedure was followed for BF photos of the C12 tags.

Intra and inter-tag distribution histograms. The FSIM indices were plotted in histogram plots to visualise the separation between the inter- and the intra-tag FSIM index distributions. The histograms were fitted to Gaussian distributions, and the overlap point between the two Gaussian distributions was estimated and assumed as the threshold for authentication ($\text{Threshold}_{\text{FSIM}}$). The FPR was estimated as the area delimited between the $\text{Threshold}_{\text{FSIM}}$ value and the inter-tag similarity distribution. The FNR was estimated as the area delimited between the intra-tag similarity distribution and the $\text{Threshold}_{\text{FSIM}}$ value^{52,53}.

All calculations and graphical representations were done using custom-made Python scripts and functions from libraries such as Scipy, Numpy, Matplotlib, OpenCV and PyTorch Image Quality.

POM observation of the C12 tag optical response to acetic acid and acetone vapours

A C12 film was placed in a hermetic and transparent glass chamber mounted on the microscope stage, between the crossed polarisers, and connected to a custom-made vapour delivery system, which was used to alternately expose the film to acetic acid vapours (or acetone vapours) and ambient air^{18,20,44}. More specifically, acetic acid or acetone (15 mL) was heated for 15 min in a glass vial immersed in a water bath at 37°C to generate a saturated atmosphere with acetic acid or acetone vapours. The headspace of the vial was pumped into the film glass chamber (during 10 s) alternately with ambient air (during 40 s). Simultaneously, the optical changes of the film were observed by POM. The Bandicam screen recorder software was used to record, in video format, the droplets’ optical textures changes during the exposure to acetic acid or acetone and air. Using the Fiji software (ImageJ 1.54p version)⁵¹, the video was converted into a sequence of images, which were represented as a function of time to show the representative optical texture changes of the film during exposure to the volatile molecules and ambient air.

Assessment of the tamper-evidence properties of the C12 tag

Three experiments were performed to demonstrate the tamper-evidence characteristics of C12 films. First, a C12 film spread over a glass slide was covered with a microscope coverslip, and finger pressure was applied. The film with the coverslip was imaged by POM and BF microscopy before and after finger-pressing. In the second experiment, a C12 gel was left to gelate inside a transparent glass vial, forming a detachable membrane with the shape of the vial. The C12 membrane formed on the bottom of the vial was observed by POM before and after being detached from the vial. Finally, a scotch-like transparent tape was applied onto a glass slide, and the C12 gel was spread on top of it. After gelating, the C12 film was imaged by POM before and after detaching the tape from the glass slide.

Characterisation of the optical response of the C12 tag to temperature

The thermal behaviour of the C12 tag was investigated using an Axioskop 40 microscope (Zeiss, Germany) equipped with a Linkam hotstage, and an Axiocam 503 colour camera. Photographs taken were processed by the ZEN 203 software (Zeiss, Germany). A C12 film was subjected to a heating ramp from 23°C to 40°C (rate of $3^\circ\text{C}/\text{min}$ from 23°C to 33°C and 37°C to 40°C ; and rate of $0.1^\circ\text{C}/\text{min}$ from 33°C to 37°C) and cooled back to 23°C at the same rates to assess the ordering and phase transitions of the LC and the reversibility of LC droplet radial configuration. To investigate the repeatability of the optical response, this heat/cool cycle was applied twice to a single C12 film. POM and BF photographs were taken during heating and cooling.

Data availability

The data generated and analysed in this study, namely the BF images used for droplet size distribution calculation, the ionogels' rheometry, compressive and tensile data, the ionogels' weight variation at room conditions, the POM and BF images used for the long term morphology stability analysis of C12 films, the POM and BF images of C12 tags used for the calculation of intra and inter-tag similarity analysis, and the dataset of C12 tag's optical signals to VOCs used to train and test the VOC classification model, are subjected to controlled access to safeguard intellectual property. These data will be provided (for academic use only) upon request by e-mail to the authors SICJP (s.palma@fct.unl.pt) and ACAR (cecilia.roque@fct.unl.pt).

Code availability

All the scripts for image data processing (droplet size distribution, morphological stability assessment, C12 tag intra and inter-tag similarity), for optical signal pre-processing and for the VOC classification model training and testing will be provided (for academic use only) upon request by e-mail to the authors SICJP (s.palma@fct.unl.pt) and ACAR (cecilia.roque@fct.unl.pt). The scripts were written using Python 3.8.5 version, along with its libraries Scipy (version 1.9.1), Numpy (version 1.24.4), Matplotlib (3.3.2), pandas (version 1.1.3), OpenCV (cv2, version 4.8.1), PyTorch (version 2.1.0+cpu) and PyTorch Image Quality (version piq 0.8.0).

Received: 13 February 2025; Accepted: 3 September 2025;

Published online: 30 September 2025

References

- Arppe, R. & Sørensen, T. J. Physical unclonable functions generated through chemical methods for anti-counterfeiting. *Nat. Rev. Chem.* **1**, 1–13 (2017).
- OECD & European Union Intellectual Property Office. *Global Trade in Fakes: A Worrying Threat*, OECD (2021).
- Pappu, R., Recht, B., Taylor, J. & Gershenfeld, N. Physical one-way functions. *Science* **2097**, 2026–2030 (2002).
- Moglianetti, M. et al. Nanocatalyst-enabled physically unclonable functions as smart anticounterfeiting tags with AI-aided smartphone authentication. *ACS Appl. Mater. Interfaces* **14**, 25898–25906 (2022).
- Liu, Y. et al. Inkjet-printed unclonable quantum dot fluorescent anti-counterfeiting labels with artificial intelligence authentication. *Nat. Commun.* **10**, 2409 (2019).
- Geng, Y. et al. High-fidelity spherical cholesteric liquid crystal Bragg reflectors generating unclonable patterns for secure authentication. *Sci. Rep.* **6**, 26840 (2016).
- Buchanan, J. D. R. et al. Forgery: 'Fingerprinting' documents and packaging. *Nature* **436**, 475 (2005).
- Park, G., Park, H., Wolska, J. M., Park, J. G. & Yoon, D. K. Racemized photonic crystals for physical unclonable function. *Mater. Horiz.* **9**, 2542–2550 (2022).
- Bruno, M. D. L. et al. Cholesteric liquid crystals based micro-fingerprints generator for anti-counterfeiting labels. *Adv. Mater. Technol.* **8**, 2300613 (2023).
- Kim, J. H. et al. Nanoscale physical unclonable function labels based on block copolymer self-assembly. *Nat. Electron.* **5**, 433–442 (2022).
- Sun, N. et al. Random fractal-enabled physical unclonable functions with dynamic AI authentication. *Nat. Commun.* **14**, 2185 (2023).
- Sun, H., Maji, S., Chandrakasan, A. P. & Marelli, B. Integrating biopolymer design with physical unclonable functions for anticounterfeiting and product traceability in agriculture. *Sci. Adv.* **9**, eadf1978 (2023).
- Park, S. M., Park, G. & Yoon, D. K. Paintable physical unclonable functions using DNA. *Adv. Mater.* **35**, 2302135 (2023).
- Park, G., Choi, Y.-S., Kwon, S. J. & Yoon, D. K. Planar spin glass with topologically protected mazes in the liquid crystal targeting for reconfigurable micro security media. *Adv. Mater.* **35**, 2303077 (2023).
- Kim, K. et al. Voxellated opto-physically unclonable functions via irreproducible wrinkles. *Light Sci. Appl.* **12**, 245 (2023).
- Park, J.-S. et al. Physical unclonable functions employing circularly polarized light emission from nematic liquid crystal ordering directed by helical nanofilaments. *ACS Appl. Mater. Interfaces* **16**, 7875–7882 (2024).
- Hussain, A. et al. Tunable gas sensing gels by cooperative assembly. *Adv. Funct. Mater.* **27**, 1700803 (2017).
- Frazão, J. L. et al. Optical gas sensing with liquid crystal droplets and convolutional neural networks. *Sensors* **21**, 2854 (2021).
- Esteves, C. et al. Effect of film thickness in gelatin hybrid gels for artificial olfaction. *Mater. Today Bio.* **1**, 100002 (2019).
- Esteves, C. et al. Tackling humidity with designer ionic liquid-based gas sensing soft materials. *Adv. Mater.* **34**, 2107205 (2022).
- Moreira, I. P., Sato, L., Alves, C., Palma, S. & Roque, A. C. Fish gelatin-based films for gas sensing. In *BIODEVICES 2021 – 14th International Conference on Biomedical Electronics and Devices; Part of the 14th International Joint Conference on Biomedical Engineering Systems and Technologies, BIOSTEC 2021*, 32–39 (2021).
- Ramou, E., Palma, S. I. C. J. & Roque, A. C. A. Nanoscale events on cyanobiphenyl-based self-assembled droplets triggered by gas analytes. *ACS Appl. Mater. Interfaces* **14**, 6261–6273 (2022).
- Ramou, E. & Roque, A. C. Textural landscapes of VOC-sensitive chiral liquid crystal-based materials. *Appl. Phys. Rev.* **10**, 011411 (2023).
- Oliveira, A. R., Costa, H. M. A. A., Ramou, E., Palma, S. I. C. J. C. J. & Roque, A. C. A. Effect of polymer hydrophobicity in the performance of hybrid gel gas sensors for E-noses. *Sens.* **23**, 3531 (2023).
- Oliveira, A. R. et al. Impact of the cationic moiety of ionic liquids on chemoselective artificial olfaction. *ACS Mater. Au* **3**, 678–686 (2023).
- Rawat, K., Pathak, J. & Bohidar, H. B. Effect of solvent hydrophobicity on gelation kinetics and phase diagram of gelatin ionogels. *Soft Matter* **10**, 862–872 (2014).
- Pei, M. S., Wu, Z. Y., Wang, L. Y., Wu, X. Z. & Tao, X. T. Phase behavior of liquid crystals formed in [C₁₂mim]Cl/H₂O and [C₁₂mim]Cl/alcohols systems. *Chin. J. Chem. Phys.* **22**, 453–459 (2009).
- Goodchild, I. et al. Structural studies of the phase, aggregation and surface behaviour of 1-alkyl-3-methylimidazolium halide + water mixtures. *J. Colloid Interface Sci.* **307**, 455–468 (2007).
- Saouane, S. & Fabbiani, F. P. A. Structural behavior of long-chain imidazolium-based ionic liquid [C₁₀mim]Cl–water mixtures. *Cryst. Growth Des.* **15**, 3875–3884 (2015).
- Vidinha, P. et al. Ion jelly: a tailor-made conducting material for smart electrochemical devices. *Chem. Commun.* **44**, 5842–5844 (2008).
- Moreira, I. P. et al. Synergy between silk fibroin and ionic liquids for active gas-sensing materials. *Mater. Today Bio.* **15**, 100290 (2022).
- Crespo, E. A., Schaeffer, N., Coutinho, J. A. P. & Perez-Sanchez, G. Improved coarse-grain model to unravel the phase behavior of 1-alkyl-3-methylimidazolium-based ionic liquids through molecular dynamics simulations. *J. Colloid Interface Sci.* **574**, 324–336 (2020).
- Prishchepa, O. O., Zyryanov, V. Y., Gardymova, A. P. & Shabanov, V. F. Optical textures and orientational structures of nematic and cholesteric droplets with heterogeneous boundary conditions. *Mol. Cryst. Liquid Cryst.* **489**, 84/[410]–93/[419] (2008).
- Tariq, M. et al. Surface tension of ionic liquids and ionic liquid solutions. *Chem. Soc. Rev.* **41**, 829–868 (2012).
- Drzaic, P. S. Nematic configurations within droplets. In *Liquid Crystal Dispersions* Vol. 152 (WORLD SCIENTIFIC, Singapore, 1995).
- Yang, J. D. Birefringence patterns of nematic droplets. *Jpn. J. Appl. Phys.* **31**, 2837 (1992).
- Gupta, J. K., Zimmerman, J. S., De Pablo, J. J., Caruso, F. & Abbott, N. L. Characterization of adsorbate-induced ordering transitions of liquid crystals within monodisperse droplets. *Langmuir* **25**, 9016–9024 (2009).
- Carlton, R. J., Zayas-Gonzalez, Y. M., Manna, U., Lynn, D. M. & Abbott, N. L. Surfactant-induced ordering and wetting transitions of droplets of thermotropic liquid crystals "Caged" inside partially filled polymeric capsules. *Langmuir* **30**, 14944–14953 (2014).

39. Ondris-Crawford, R. et al. Microscope textures of nematic droplets in polymer dispersed liquid crystals. *J. Appl. Phys.* **69**, 6380–6386 (1991).
40. Lopez-Leon, T. & Fernandez-Nieves, A. Drops and shells of liquid crystal. *Colloid Polym. Sci.* **289**, 345–359 (2011).
41. Wang, X., Bukusoglu, E. & Abbott, N. L. A practical guide to the preparation of liquid crystal-templated microparticles. *Chem. Mater.* **29**, 53–61 (2017).
42. Ramou, E., Rebordão, G., Palma, S. I. C. J. & Roque, A. C. A. Stable and oriented liquid crystal droplets stabilized by imidazolium ionic liquids. *Molecules* **26**, 6044 (2021).
43. Zhang, L., Zhang, L., Mou, X. & Zhang, D. FSIM: a feature similarity index for image quality assessment. *IEEE Trans. Image Process.* **20**, 2378–2386 (2011).
44. Ramou, E., Palma, S. I. C. J. & Roque, A. C. A. A room temperature 9CB-based chemical sensor. *Nano Sel.* **4**, 525–536 (2023).
45. Esteves, C. et al. VOC sensing in humid and dry environments. In *2022 IEEE International Symposium on Olfaction and Electronic Nose (ISOEN)*, 1–3 (IEEE, 2022).
46. Zhang, M., Raghunath, A., Zhao, A. & Eral, H. B. Biocompatible optical physically unclonable function hydrogel microparticles for on-dose authentication. *Heliyon* **10**, e22895 (2024).
47. Esidir, A. et al. Food-grade physically unclonable functions. *ACS Appl. Mater. Interfaces* **15**, 41373–41384 (2023).
48. Carro-Temboury, M. R., Arppe, R., Vosch, T. & Sørensen, T. J. An optical authentication system based on imaging of excitation-selected lanthanide luminescence. *Sci. Adv.* **4**, e1701384 (2018).
49. ISO. *International Organization of Standards* Vol. 20897 (ISO/IEC, 2020).
50. Cardona, A. et al. TrakEM2 software for neural circuit reconstruction. *PLoS One* **7**, e38011 (2012).
51. Schindelin, J. et al. Fiji: an open-source platform for biological-image analysis. *Nat. Methods* **9**, 676–682 (2012).
52. Moon, C. et al. Anticounterfeiting tags based on randomly oriented MoS_x clusters enabled by capillary and marangoni flow. *Commun. Mater.* **4**, 98 (2023).
53. Meijis, Z. C. et al. Pixelated physical unclonable functions through capillarity-assisted particle assembly. *ACS Appl. Mater. Interfaces* **15**, 53053–53061 (2023).
54. Zannoni, C. *Liquid Crystals and Their Computer Simulations* (Cambridge University Press, Cambridge UK, 2022).
55. Dierking, I. *Textures of Liquid Crystals* (John Wiley & Sons, 2003).
56. Schelski, K., Reyes, C. G., Pschyklien, L., Kaul, P. M. & Lagerwall, J. P. F. Quantitative volatile organic compound sensing with liquid crystal core fibers. *Cell Rep. Phys. Sci.* **2**, 100661 (2021).
57. Kastyulin, S., Zakirov, D. & Prokopenko, D. PyTorch image quality: metrics and measure for image quality assessment. Preprint at <https://doi.org/10.48550/arXiv.2208.14818> (2022).

Acknowledgements

The authors acknowledge funding from European Research Council under the EU Horizon 2020 research and innovation programme (grant agreement no. SCENT-ERC-2014-STG-639123, 2015–2022, grant agreement no. 101069405-ENSURE-ERC-2022-POC1, and 101158248-UNMASK-ERC-2023-POC). We also thank funding from Fundação para a Ciência e Tecnologia, I.P. (FCT), in the scope of the SUTBLE project, ref 2023.12656.PEX and the projects PTDC/CTM-CTM/3389/2021, UIDP/04378/2020, and UIDB/04378/2020 of the Research Unit on Applied Molecular Biosciences—UCIBIO, project LA/P/0140/2020 of the Associate Laboratory Institute for Health and Bioeconomy—i4HB. We also acknowledge funding from Plano de Recuperação e Resiliência (PRR)—

RE-C05-i01.01—Agendas/Aliaças mobilizadoras para a Inovação Empresarial (Portugal) under the project “HfPT—Health from Portugal” (project code C630926586-00465198). The authors thank Dr. Ana Luísa Carvalho (UCIBIO, at NOVA University Lisbon, Portugal) for undertaking the X Ray diffraction experiments; Dr. Tomás Calmeiro (CENIMAT, at NOVA FCT) for the AFM images; Prof. Ana Rita Duarte (LAQV, at NOVA FCT) for providing access to the Rheometer equipment; Dr. Diana Araújo, Francisco Santos and Prof. Filomena Freitas (UCIBIO, at NOVA FCT) for the assistance with tensile and compressive assays; Dr. Ana Marques and Prof Isabel Ferreira (DCM, at NOVA FCT) for the Raman scanning and AFM images of C12 films, and Dr. Carina Esteves (UCIBIO, at NOVA FCT) for helpful discussions.

Author contributions

S.I.C.J.P. performed the experiments, analysed the data, designed the figures, and wrote the manuscript. E.R. assisted in the LC-related experiments, contributed to the data analysis and revised the manuscript. A.C.A.R. conceived the idea, designed the experiments, supervised the project, supported the project, including funding support, and revised the manuscript.

Competing interests

The authors declare no competing interests.

Additional information

Supplementary information The online version contains supplementary material available at <https://doi.org/10.1038/s43246-025-00940-x>.

Correspondence and requests for materials should be addressed to Ana C. A. Roque.

Peer review information *Communications Materials* thanks Dong Ki Yoon and the other, anonymous, reviewer(s) for their contribution to the peer review of this work. A peer review file is available.

Reprints and permissions information is available at <http://www.nature.com/reprints>

Publisher's note Springer Nature remains neutral with regard to jurisdictional claims in published maps and institutional affiliations.

Open Access This article is licensed under a Creative Commons Attribution-NonCommercial-NoDerivatives 4.0 International License, which permits any non-commercial use, sharing, distribution and reproduction in any medium or format, as long as you give appropriate credit to the original author(s) and the source, provide a link to the Creative Commons licence, and indicate if you modified the licensed material. You do not have permission under this licence to share adapted material derived from this article or parts of it. The images or other third party material in this article are included in the article's Creative Commons licence, unless indicated otherwise in a credit line to the material. If material is not included in the article's Creative Commons licence and your intended use is not permitted by statutory regulation or exceeds the permitted use, you will need to obtain permission directly from the copyright holder. To view a copy of this licence, visit <http://creativecommons.org/licenses/by-nc-nd/4.0/>.

© The Author(s) 2025